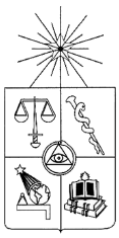

UNIVERSIDAD DE CHILE
FACULTAD DE CIENCIAS FÍSICAS Y MATEMÁTICAS
DEPARTAMENTO DE INGENIERÍA ELÉCTRICA
DEPARTAMENTO DE INGENIERÍA INDUSTRIAL

DISEÑO Y DESARROLLO DE UN SISTEMA PARA LA DETECCIÓN AUTOMÁTICA DE RETINOPATÍA DIABÉTICA EN IMÁGENES DIGITALES

MEMORIA PARA OPTAR A LOS TÍTULOS DE
INGENIERO CIVIL ELECTRICISTA E
INGENIERO CIVIL INDUSTRIAL

JOSÉ TOMÁS ARENAS CAVALLI

PROFESOR GUÍA:
MARIANO POLA MATTE

MIEMBROS DE LA COMISIÓN:
SEBASTIÁN RÍOS PÉREZ
CLAUDIO ESTÉVEZ MONTERO
CARLOS REVECO DÍAZ

SANTIAGO DE CHILE
MAYO 2012

RESUMEN DE LA MEMORIA
PARA OPTAR A LOS TÍTULOS DE
INGENIERO CIVIL ELECTRICISTA E
INGENIERO CIVIL INDUSTRIAL
POR: JOSÉ TOMÁS ARENAS CAVALLI
FECHA: 22/05/2012
PROF. GUÍA: MARIANO POLA MATTE

DISEÑO Y DESARROLLO DE UN SISTEMA PARA LA DETECCIÓN AUTOMÁTICA DE RETINOPATÍA DIABÉTICA EN IMÁGENES DIGITALES

La detección automática de la patología oftalmológica denominada retinopatía diabética tiene el potencial de prevenir casos de pérdida de visión y ceguera, en caso de impulsar la examinación masiva de pacientes con diabetes. Este trabajo apunta a diseñar y desarrollar un clasificador a nivel de prototipo que permita discriminar entre pacientes con y sin presencia de la enfermedad, por medio del procesamiento automático de imágenes de fondo de ojo digitales. Los procedimientos se basan en la adaptación e integración de algoritmos publicados.

Las etapas desarrolladas en el procesamiento digital de las imágenes de retina para este objetivo fueron: localización de vasos sanguíneos, localización de disco óptico (DO), detección de lesiones claras y detección de lesiones rojas. Las técnicas utilizadas para cada una de las etapas fueron, respectivamente: *Gabor wavelets* y clasificadores bayesianos; características de los vasos y predicción de posición mediante regresores kNN; segmentación mediante *fuzzy c-means* y clasificación usando una red neuronal multicapas; y, operadores morfológicos ajustados óptimamente.

La base de datos de imágenes para el entrenamiento y prueba de los métodos desarrollados cuenta con 285 imágenes de un centro médico local, incluyendo 214 normales y 71 con la enfermedad. Los resultados específicos fueron: 100% de precisión en la ubicación del DO en las 142 imágenes de prueba; identificación del 91,4% de las imágenes con lesiones claras, i.e., la sensibilidad, mientras se reconocieron 53,3% de las imágenes sin lesiones claras, i.e., la especificidad (84,1% de sensibilidad y 84,7% de especificidad a nivel de pixel) en las mismas 142 muestras; y, 97% de sensibilidad y 92% de especificidad en la detección de lesiones rojas en 155 imágenes. El desempeño en la ubicación de la red vascular es medido por el resultado del resto de los pasos. El rendimiento general del sistema es de un 88,7% y 49,1% en cuanto a sensibilidad y especificidad, respectivamente.

Algunas medidas fundamentales son necesarias para la implementación a futuro. En primer lugar, acrecentar la base de datos de imágenes para entrenamiento y prueba. Además, es posible pulir cada una de las etapas intermedias de las cuatro grandes fases. Con todo, una ronda de implementación a nivel usuario de un prototipo general permitirá evaluación y mejora de los métodos diseñados y desarrollados.

DESIGN AND DEVELOPMENT OF A SYSTEM FOR AUTOMATED DETECTION OF DIABETIC RETINOPATHY IN DIGITAL IMAGES

Automated detection of the ophthalmologic pathology known as diabetic retinopathy has the potential of preventing vision loss and blindness cases, when promoting massive screening of diabetic patients. This work aims to design and develop a functional classifier at a prototype level, allowing to discriminate between patients with and without presence of the disease by means of automated digital eye fundus images processing. Procedures are based in adaptation and integration of publicly available algorithms.

Digital retina images processing developed stages were: blood vessels localization, optic disc (OD) localization, bright lesions detection and red lesions detection. For each one of the stages, used techniques were, respectively: Gabor wavelets and Bayesian classifiers; vessel features and kNN regressors position prediction; fuzzy c-means segmentation and multilayer neural network classification; and, optimally adjusted morphological operators.

Training and test image database for developed methods considers 285 local health center images, including 214 normal and 71 abnormal ones. Specific results were: 100% precision in OD localization in the 142 testing images; identification of 91.4% of bright lesions images, i.e., sensitivity, while recognizing 53.3% of images without bright lesions, i.e., specificity (84.1% sensitivity and 84.7% specificity at a pixel level) in the same 142 samples; and, 97% sensitivity and 92% specificity in red lesions detection in 155 images. Vasculature localization performance is measured by the rest of the steps result. Overall system performance reaches 88.7% and 49.1% in terms of sensitivity and specificity, respectively.

Regarding future implementation, some key actions are necessary. First, training and test database growth. Besides, fine tunning of each main intermediate stage is possible. Thus, a general prototype user-level round of implementation will allow designed and developed methods evaluation and improvement.

A mi madre, Rossana.

Acknowledgements

I would like to thank my advisory committee, specially Mariano Pola and Sebastián Ríos, who devoted much time to support this project through weekly meetings and significant guidelines. This thesis certainly would not have been possible without their help and dedication, in addition to all the people involved thanks to their management.

I would also like to thank all my friends, who have accompanied me from the first day of university until the end of this important and, at times, difficult stage. Thanks for making the tough times bearable and for all the great experiences throughout all these years.

Last, but not least, I thank my family for always being there and believing in my capabilities and ambitions. I definitely could not have crossed not only this last step, but the whole education road, if not for their love and confidence in me.

Contents

List of Figures

List of Tables

Chapter 1

Introduction

Digital image processing is useful for two major purposes: improvement of information for human interpretation and automated machine analysis. Specifically, adequate image processing complemented with classification methods has many medical applications. Therefore, an automated system that integrates this concepts may provide a successful non-supervised stage in disease screening.

1.1 Context

Diabetic Retinopathy (DR) is an ocular complication of diabetes. It is the most common cause of blindness among adults aged greater than 65 years in the developed countries and among adults aged between 20 and 74 years in the United States (U.S.) [1–4]. It affects working population of the European Union and the U.S. [5], blinding about 25,000 patients with diabetes annually in the U.S. alone [6]. Although early detection and laser treatment of DR have proved effective in preventing visual loss [7, 8], many diabetic patients are not treated in time because of inadequacies of the currently available screening programs [9, 10]. This applies to almost 50% of the 18 million patients with diabetes in the U.S who do not undergo any form of regular documented dilated eye exam [11–14], as illustrated in Fig 1.1.

There is overwhelming scientific evidence that supports early detection, combined with proper management, can prevent up to 95% of cases of vision loss and blindness [15–22]. There are also guidelines of the American Diabetes Association (ADA) and the American Academy of Ophthalmology (AAO) that advise an annual dilated eye exam for most patients with diabetes [23–25]. A major limiting factor is the scale required for a screening program for the entire population of diabetics.

Digital photography of the retina examined by ophthalmologists or other qualified readers has been shown to have sensitivity and specificity comparable with or better than indirect ophthalmoscopy by an ophthalmologist [26, 27] (sensitivity: probability of a positive test given that the patient is ill; specificity: probability of a negative test given that the patient is well) and has been proposed as an approach to make the dilated eye exam available to underserved populations that do not receive regular exams by ophthalmologist. If all of these populations in the U.S. were to be served with digital imaging, the number of retinal images to be evaluated annually is 32 million (about 50% of patients with diabetes and at least two photographs per eye) [27, 28]. In France, this technique was approved as a standard reference because of its high sensitivity in detecting retinal lesions [26, 29, 30].

Current aging rate of Chilean population allows to project these figures to a local level; the type of diseases that affect it has changed from infectious to chronic, such as diabetes. This fact should be of concern, taking into account age-related statistics (Table 1.1). It is in this context it is noteworthy that there are no programs supported by automation as those mentioned above and the opportunity to move in the direction of developed countries arises.

1.2 Motivation

There is a business opportunity because of the increasing percentage of the diabetic population in Chile and the world, besides implications of eye problems. Between 2005 and 2008, 4.2 million (28.5%) of individuals aged 40 and older with diabetes in the U.S. had DR. Of these, 655,000 (4.4% of those with diabetes) had advanced DR that could lead to severe loss of vision [31]. In Chile, year 2002 census confirms a

Table 1.1: Diagnosed (and undiagnosed) diabetes among people ages 20 years or older, United States, 2010 [31]

Group	Number or percentage who have diabetes
Ages 20 years or older	25.6 million, or 11.3 percent, of all people in this age group
Ages 65 years or older	10.9 million, or 26.9 percent, of all people in this age group
Men	13.0 million, or 11.8 percent, of all men ages 20 years or older
Women	12.6 million, or 10.8 percent, of all women ages 20 years or older

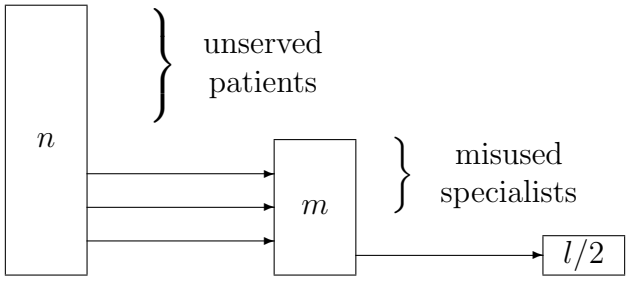

Figure 1.1: Current annual situation. n patients attempt to get served by specialists with availability for m. Only $l/2$ of the served patients are actually affected by the condition. $m \simeq 0.5n$ and $l/2 \simeq 0.29m$; hence, $l/2 \simeq 0.1425n$. Equivalently, 14.25% of the n diabetic patients may have undiagnosed DR.

decrease in the percentage of children under fifteen years old versus elderly, varying the aging index (number of people aged 60 years or older for every hundred children under 15 years old) of 46.06 in 2005 to a projection of 119 in 2030. Therefore, it becomes essential to address related conditions with new strategies [32].

On the other hand, the congestion of the public system to meet the demand for these kind of tests is concerning. This adds to the annually suggested revision and the total coverage of the disease by the national health program *Acceso Universal a Garantías Explícitas* (AUGE) [33], which is difficult to accomplish considering a gap of approximately three months from the booking of an appointment until it takes place. Aware of the above, the aim is to contribute towards health challenges Chile faces nowadays [34].

With this opportunity in mind, a project of massive DR detection service using technology and data processing of global state of the art is born. The service is based on a system to automate the preliminary diagnosis classification of the of early detection of DR. The input data is a captured digital image, corresponding to the non-mydriatic camera retinography. The project consists of conducting its business plan and its full development in terms of digital processing. This degree work is focused in this last part. Thus, the problem is reduced to develop a prototype of a classifier that allows to rule out cases of apparent absence of the disease (minimizing false negatives), leading patients with potential complications to specialists, effectively (Fig. 1.2).

The direct customer of this work is the company *Micrológica Innovación S.A.*, represented by Mr. Mariano Pola. *Micrológica Innovación* is a company that aims to seed, incubate and develop technology businesses in the area of telematics (applications that integrate telecommunications and information technologies). Other forces

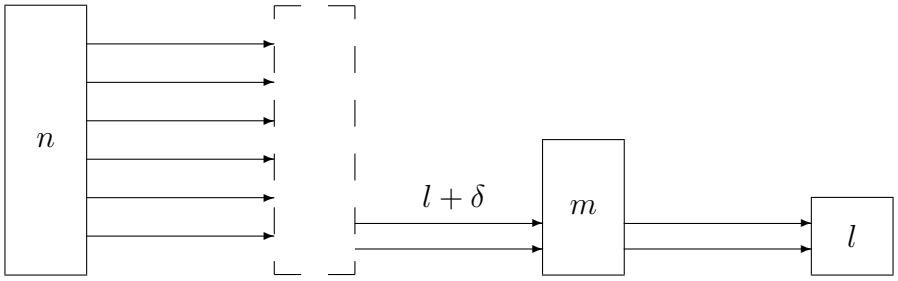

Figure 1.2: Proposed annual situation. All of the n patients get served by the system, operated by non-specialists (dashbox). All of the l DR patients, plus a security $\delta << l$, are referred to specialists to confirm or rule out DR presence.

of the project are composed by Dr. Rodrigo Donoso (eye surgeon, *Universidad de Chile*, *Clínica Oftalmológica Pasteur*), *Centro de Referencia de Salud* (CRS) *Peñalolén Cordillera Oriente* and Departments of Electrical Engineering (DIE) and Industrial Engineering (DII) at *Universidad de Chile*.

1.3 Objectives

1.3.1 General Objective

Develop a functional prototype classifier that allows to discriminate among patients with and without presence of diabetic retinopathy by means of an automated digital eye fundus images processing.

1.3.2 Specific Objectives

- Collection and preparation of a dataset for the occasion.
- Identification of state of the art techniques and selection of appropriate guidelines to particular problem.
- Algorithms implementation.
- Experimentation of the developed algorithms.
- Development of effectiveness indicators of the system which allow drawing useful conclusions for feasibility assessment.

- Design, development and implementation of a prototype to evaluate algorithms performance and indicators sensitivity.

1.4 Methodology

The methodology adopted for this project is based on the pillars of a guide to data mining, CRISP-DM [35], supplemented with concrete methodologies to address this specific problem. The coarse stages are described in Table 1.2

Business understanding phase is related with this very chapter in terms of current and proposed situation (Figs. 1.1, 1.2). Data understanding and preparation outputs are summarized in Section 3.1 and can be reviewed in particular quality filters for each development section.

Modeling stage can be described in turn as a particular methodology. It is mainly based on the concatenation of the best techniques (results, number of citations and feasibility) for each of the processes necessary to carry out the detection of DR in a digital image. This systematization is not unprecedented [12, 13] and its stages for this adaptation, whose order and relationship will be explained in Chapter 3, consist in: locating blood vessels, locating the optic disc (OD), detecting bright lesions and detecting red lesions.

Specifics of each location/detection stage, as well as their interaction and complemen-

Table 1.2: Generic tasks of the CRISP-DM reference model; first five stages [35]

Business Understanding	Data Understanding	Data Preparation	Modeling	Evaluation
Determine business objectives	Collect initial data	Select data	Select modeling techniques	Evaluate results
Assess situation	Describe data	Clean data	Generate test design	Review process
Determine data mining goals	Explore data	Construct data	Build model	Determine next steps
Produce project plan	Verify data quality	Integrate data Format data	Assess model	

tation are part of the design and therefore will be detailed in Chapter 3. Justification of techniques chosen is found in Section 2.5. According to this decision, a localization or detection may be prerequisite to another one. This will determine the proper sequence of steps in the coarse design.

Finally, CRISP-DM evaluation is mostly carried out in Chapter 4, except for intermediate outcomes that are displayed along with the implementation and next steps determination, in Chapter 5.

1.5 Thesis Structure

Besides this chapter, the following ones are revised in this section. The idea is to summarize and set out the main outcomes of each of them.

Chapter 2, Literature Review: every general aspect of theoretical knowledge is explained here, in order to understand technical matters taken for granted in further chapters. In this sense, both clinical and technological concepts must be taken into account. Diabetic Retinopathy, Image Processing and Pattern Recognition and Classification, plus a State of the Art overhaul are the primary themes that need to be fully understood, oriented to the concerned scope.

Chapter 3, Design and Implementation: as stated in the title, here is where the solution is fully designed and developed towards its results. Both stages of abnormalities detection, bright and red lesions, are fully detailed based on the chosen state of the art techniques and customized algorithms. Similarly, two morphological localizations take place: OD and blood vessels. This additional recognition serves only as a requisite for abnormalities detection. Training, validation and test phases are described, when appropriate.

Chapter 4, Results and Discussion: specific and general performance indicators are presented and compared to expected results. Threshold sensitivity analysis and possible failure reasons are reviewed, when applicable. This is, of course, the output of previous chapter and leads to next chapter closure.

Chapter 5, Conclusions and Future Work: this chapter summarizes previous ones but, mostly, the one that presents the results. Moreover, it guides further elaboration and polishing as it states potential fixes to specific design issues as well as development flaws.

Chapter 2

Literature Review

The purpose of this chapter is to familiarize the reader with certain concepts, both clinical and technical, so that reading and understanding the rest of the paper is as fluent as possible. An overview of the clinical aspects of DR disease, supported by graphical descriptions of its manifestation, is exposed. Likewise, it is followed by an overview of basic image processing notions and selected techniques. Finally, a summary of previous research is performed, analyzing the pros and cons of each approach for each goal within DR detection.

2.1 Diabetic Retinopathy

"Over decades, there has been broad interest of ophthalmologists and diabetologists in DR. Despite markedly improved prognosis for visual problems due to laser treatment and vitrectomy, DR is still one of the leading causes of blindness worldwide [36]". This section seeks to introduce briefly the basic ideas on DR, mostly base on specialized literature [37]. After reading it, the reader is expected to graphically understand retinal differences between normal and abnormal patients.

2.1.1 Retinal basic knowledge

Once looking at the retina (in an ophthalmoscopy or a fundus photograph), the OD should be identified. In a normal eye, it is a sharply defined structure with vital coloration (i.e., yellowish-orange) at the level of the retina and may have a central excavation. The central vein lies lateral to the artery; venous diameter is normally 1.5 times greater than arterial diameter. Each vascular structure should be of uniform

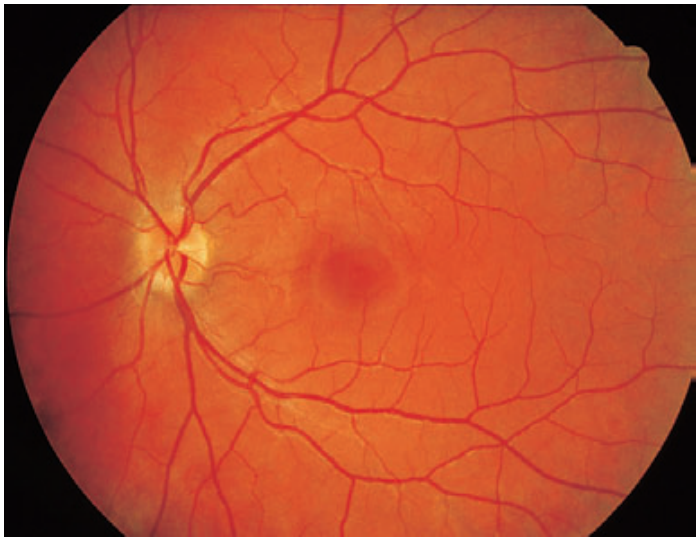

Figure 2.1: Normal fundus. The macula lutea lies about 3–4 mm temporal to and slightly below the OD. The fundus receives its uniform bright red coloration from the vessels of the choroid. The diameter of the veins is normally 1.5 times greater than that of the arteries [37].

diameter, and there should be no vascular constriction where vessels overlap. A spontaneous venous pulse is normal; an arterial pulse is abnormal. Younger patients will have a foveal and macular light reflex, and the retina will have a reddish color (see Fig. 2.1).

The macula lutea is a flattened oval area in the center of the retina approximately 3–4 mm (15°) temporal to and slightly below the OD. Its diameter is roughly equal to that of the OD (1.7–2 mm). The macula appears yellow when examined under green light, hence the name macula lutea (yellow spot). Located in its center is the avascular fovea centralis, the point at which visual perception is sharpest.

2.1.2 Examination of the fundus

Abnormal changes can be recorded with a single-lens reflex camera. This permits precise documentation of follow-up findings. Photographs obtained with a fundus camera in green light provide high-contrast images of abnormal changes to the innermost layers of the retina such as changes in the layer of optic nerve fibers, bleeding, or microaneurysms.

The EURODIAB IDDM Complications Study, conducted in Europe, showed that using a protocol of two 45° field images for each eye, a high degree of effectiveness

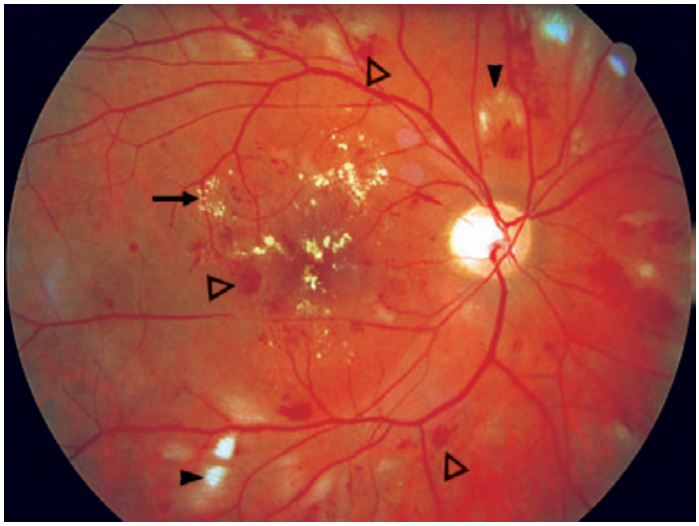

Figure 2.2: Nonproliferative diabetic retinopathy. Microaneurysms, intraretinal hemorrhage (open arrowheads); hard exudates representing lipid deposits in the retina (arrow); and cotton-wool spots representing nerve fiber infarction and soft exudates (black arrow heads) [37].

in detecting the evaluation of DR is achieved. Therefore, the homonymous protocol consists in two non-stereoscopic photographs for each eye: one macular/temporal field and one disc/nasal field.

This result is comparable to the well known gold standard; a protocol of seven stereoscopic photographic shots of 30° for each eye [38]. Thus, testing time and costs could be reduced, obtaining similar levels of sensitivity and specificity.

The nonmydriatic camera would then be a suitable screening method. It would also have the theoretical advantage of avoiding having to dilate the pupils thanks to an infrared focusing system. However, this method has been criticized for the quality of its pictures. Studies show a reduction of non-classifiable or non-valuable photographs from 26% in case of nonmydriatic up to 5% with mydriatic [39].

The protocol for retinopathy screening recommends drug use for expansion, even if a nonmydriatic camera is used [40]. Furthermore, due to various disorders in the autonomic nervous system, present in older subjects and in diabetic patients in general, there is a pupil diameter smaller than normal. In this case, the pupil size is considered as the most important factor to achieve a retinography good quality [41].

Alongside DR, different events which do not allow the classification of a retinography may occur. These are cataracts, vitreous hemorrhage, retinal detachment, among others. This must be taken into account, either as an input or as heuristics, at the

time of assuming fundus photography methods.

2.1.3 Normal fundus findings in general

The retina is normally completely transparent without any intrinsic color. It receives its uniform bright red coloration from the vasculature of the choroid (Fig. 2.1). The vessels of the choroid (vascular layer of the eye) themselves are obscured by the retinal pigment epithelium. The OD is normally a sharply defined, yellowish-orange structure (in teenagers it is pale pink, and in young children significantly paler) that may exhibit a central depression known as the optic or physiologic cup.

The OD turns pale yellow with age, and often the optic cup will become shallow and will be surrounded by a region of choroidal atrophy. The fundus will become dull and nonreflective. Drusen will be visible in the retinal pigment epithelium and middle peripheral reticular proliferations of pigment epithelium will be present.

2.1.4 Manifestation of the disease

DR is a vascular disorder; specifically, an ocular microangiopathy (affection of small blood vessels). It is one of the main causes of acquired blindness at the age of 30 to

Table 2.1: Retinal changes in nonproliferative diabetic retinopathy [37]

Stage of retinopathy	Retinal changes
1. Mild	• At least one microaneurysm, retinal hemorrhages, hard exudates
2. Moderate	• Mild intraretinal microvascular abnormalities in four quadrants of the retina • Moderate hemorrhages in two or three quadrants • Venous beading in one quadrant
3. Severe	• Moderate hemorrhages in four quadrants • Venous beading in two quadrants • Moderate IRMA in one quadrant

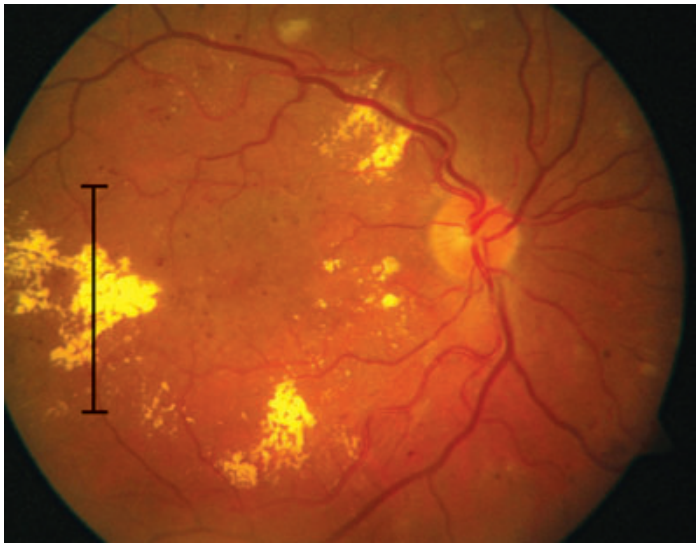

Figure 2.3: Diabetic maculopathy. Severe diabetic macular edema with hard exudates (yellow) [37].

60 years in the industrialized countries. Approximately 90% of diabetic patients have retinopathy after 20 years. The prevalence is 7%.

DR is a microangiopathy. This results in a thickening of the basement membrane of the vessels and loss of pericytes and vascular endothelial cells. Hyperglycemia, or high blood sugar, plays an important role at this early stage. Later, capillary closure occurs, resulting in retinal ischemia. The further course is triggered by hypoxia.

Diabetes mellitus can lead to changes in almost every ocular tissue. This include symptoms of several conditions. However, 90% of visual impairments in diabetic patients are caused by DR. The most common international nomenclature used to describe the various changes in DR (Table 2.1) is based on the classification of the Diabetic Retinopathy Study. A distinction is made between nonproliferative stages (1, mild; 2, moderate; 3, severe; Fig. 2.2) and proliferative stages (1, mild; 2, moderate; 3, high risk; Figs. 2.3, 2.4). Both proliferative stages and rubeosis iridis (even more sever stage) are characterized by new vessels appearance. These late stages must have been preceded by early retinal changes.

DR remains asymptomatic for a long time. Only in the late stages with macular involvement (Table 2.2) or vitreous hemorrhage will the patient notice visual impairment or suddenly go blind.

DR and its various stages (Table 2.1) are diagnosed by stereoscopic examination of the fundus with the pupil dilated. Ophthalmoscopy and evaluation of stereoscopic fundus photographs represent the gold standard.

Clinically significant macular edema (i.e., macular edema that threatens vision) is managed with focal laser treatment at the posterior pole. Proliferative DR is treated with scatter photocoagulation performed in three to five sessions (1200–1600 burns, spot size on the retina 500 μm). Vitreous hemorrhage or tractional retinal detachment are treated with vitrectomy (surgery to remove some or all of the vitreous humor from the eye).

Failure to perform regular ophthalmologic screening examinations in patients with diabetes mellitus is a negligent omission that exposes patients to the risk of blindness. All patients with type 2 diabetes should therefore receive an ophthalmologic examination on diagnosis of the disorder, and type 1 diabetic patients should receive an ophthalmologic examination within 5 years of the diagnosis. Thereafter, diabetic patients should have an ophthalmologic examination once a year, or more often if DR is present. Pregnant patients should be examined once every trimester.

Without treatment, tractional retinal detachment and macular edema can lead to severe visual impairment or blindness. However, DR can occur despite optimum therapy. Rubeosis iridis (neovascularization in the iris) in proliferative DR is tantamount to loss of the eye, as rubeosis iridis is a relentless and irreversible process.

The risk of blindness due to DR can be reduced by optimum control of blood glucose, regular ophthalmologic examination, and timely therapy, but it cannot be completely eliminated.

Table 2.2: Retinal findings in diabetic maculopathy [37]

Stage of maculopathy	Retinal findings
Clinically significant macular edema (CSME) (Fig. 2.3)	• Thickening of the retina at or within 500 μm of the center of the macula • Hard exudates at or within 500 μm of the center of the macula associated with thickening of the adjacent retina • A zone or zones of thickening one disc area or larger, any part of which is within one disc diameter of the center of the macula
Ischemic maculopathy	• Enlargement of foveal avascular zone caused by capillary closure (leads to visual impairment)

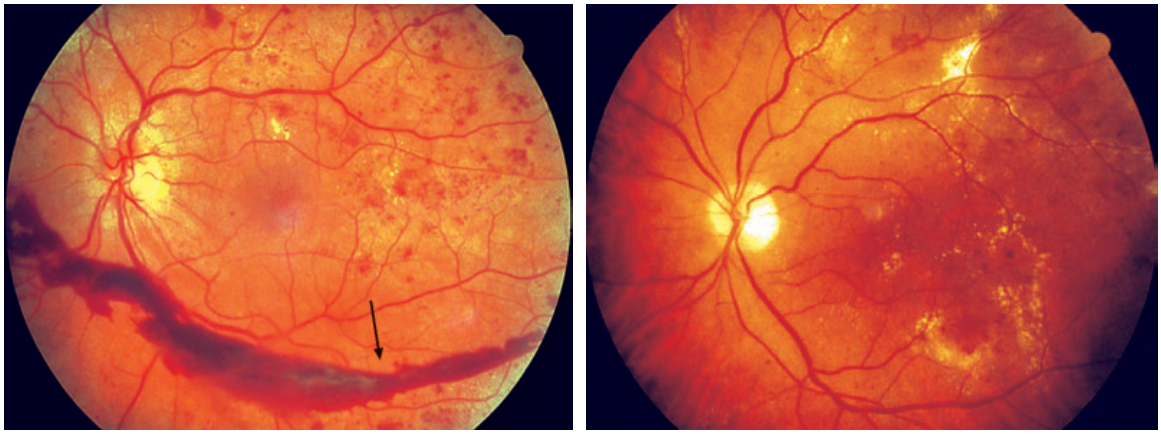

(a) (b)

Figure 2.4: Proliferative diabetic retinopathy. (a) The clearly visible vitreous hemorrhage seen here (arrow) is a typical sign of the high-risk stage of diabetic retinopathy. The patient will only notice deterioration of vision at this later stage. (b) Proliferative diabetic retinopathy with clinically significant macular edema before laser therapy [37].

2.2 Image Processing

A general introduction to color notions is presented. It is followed by description of widely used processing techniques and some more specific procedures. Everything here shown is extracted from well known authors [42].

2.2.1 Color spaces

Conversion from RGB (the brightness of the individual red, green, and blue signals, as captured by the camera and stored in the computer) to other color encoding schemes used in monitors is straightforward and loses no information except for possible round-off errors (losses do occur, however, when the color signals are broadcast with limited bandwidth). For example, Luv or CIELUV color space combines the red, green and blue signals in proportion to the human eye's perception of them. The conversion between Luv and RGB requires an intermediate step through XYZ (CIE 1931) color space [43], shown in (2.1). A more complex conversion from XYZ to Luv (CIE 1976) is needed afterwards [44].

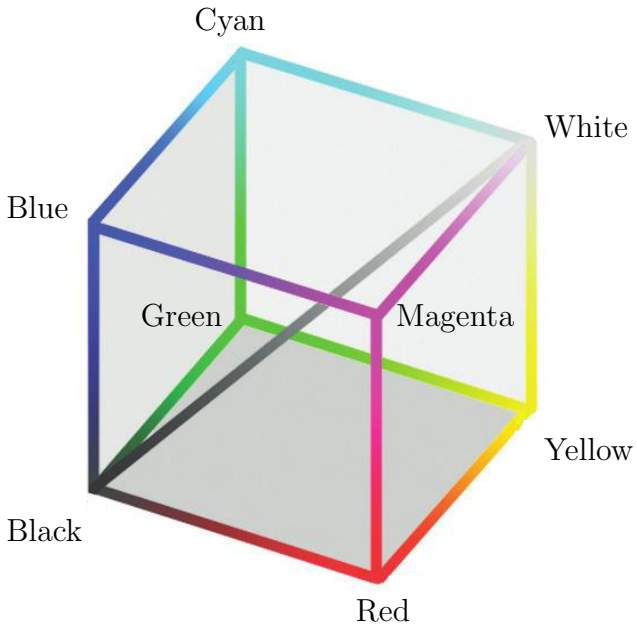

Figure 2.5: RGB Color Space. Combining Red and Green produces Yellow, Green plus Blue produces Cyan, and Blue plus Red produces Magenta. Grays lie along the cube diagonal from Black to White with equal proportions of Red, Green, and Blue. Cyan, Yellow, and Magenta are subtractive primaries used in printing, which are subtracted from White (the paper color) leaving Red, Blue and Green, respectively [42].

$$\begin{bmatrix} X \\ Y \\ Z \end{bmatrix} = \frac{1}{0.17697} \cdot \begin{bmatrix} 0.49 & 0.31 & 0.20 \\ 0.17697 & 0.81240 & 0.01063 \\ 0.00 & 0.01 & 0.99 \end{bmatrix} \cdot \begin{bmatrix} R \\ G \\ B \end{bmatrix} \tag{2.1}$$

Fig. 2.5 shows the "space" defined by RGB signals: it is a cartesian cubic space, since the red, green, and blue signals are independent and can be added to produce any color within the cube. There are other encoding schemes that are more useful for image processing and more closely related to human perception.

The *Commission Internationale de L'Éclairage* (CIE) chromaticity diagram is a two-dimensional plot defining color, shown in Fig. 2.6. The third (perpendicular) axis is the luminance, which corresponds to the panchromatic brightness which, like the Y value in YUV, produces a monochrome (gray scale) image. The two primary color axes shown, called x and y, are always positive and combine to define any color that can be seen.

The CIE diagram provides a means for color definition, but corresponds neither to the operation of hardware nor directly to human vision. An approach that does

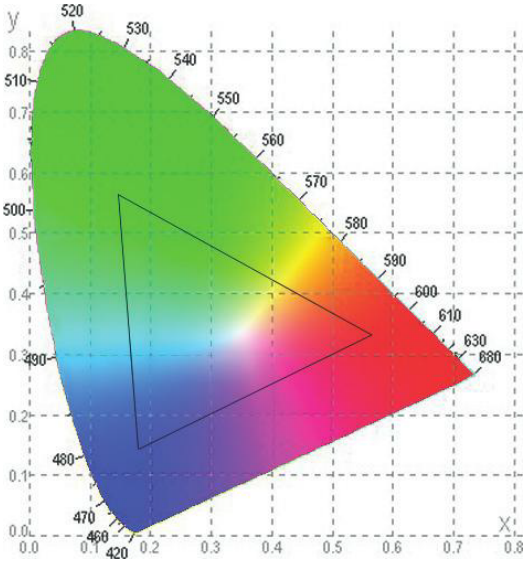

Figure 2.6: The CIE chromaticity diagram. The colors are fully saturated along the edge. Numbers give the wavelength of light in nanometers. The inscribed triangle shows the colors that typical color cathode ray tube (CRT) displays can produce by mixing of red, green, and blue light from phosphors [42].

is embodied in the HSV (hue, saturation, and value), HSI (hue, saturation, and intensity), and HLS (hue, lightness, and saturation) coordinate systems. These are closely related to each other and to the artist's concept of tint, shade, and tone. In this system, hue is what most people mean by color, for instance the distinction between red and yellow. Saturation is the amount of the color that is present, for instance the distinction between red and pink. The third axis (called lightness, intensity, or value) is the amount of light, the distinction between a dark red and light red or between dark gray and light gray.

The space in which these three values is plotted can be shown as a circular or hexagonal cone or double cone, or sometimes as a sphere or cylinder. It is most useful to picture the space as a double cone, in which the axis of the cone is the gray scale progression from black to white, distance from the central axis is the saturation, and the direction is the hue, with the primary RGB colors spaced 120° apart. Fig. 2.7 shows this concept schematically. This space has many advantages for image processing and for understanding color. For instance, if the algorithms presented in Section 2.2.2, such as spatial smoothing or median filtering, are used to reduce noise in an image; applying them to the RGB signals separately causes color shifts in the result, but applying them to the HSI or HSV components does not. Conversion from RGB to HSV can be performed directly [45].

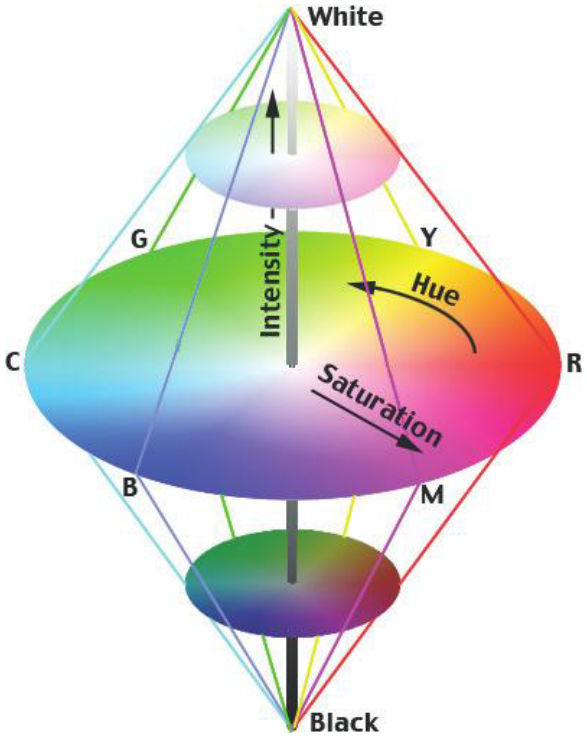

Figure 2.7: Bi-conic representation of Hue-Saturation-Intensity Space. Grays lie along the central axis. Distance from the axis gives the Saturation, while direction (angle) specifies the Hue [42].

Color images are typically digitized as 24 bit RGB, meaning that 8 bits or 256 (linear) levels of brightness for red, green, and blue are stored. This is enough to allow display on video or computer screens, or for printing purposes, but, depending on the dynamic range of the data may not be enough to adequately measure small variations within the image.

2.2.2 Correcting imaging defects: neighborhood averaging

When images are acquired under different lighting conditions, the color values recorded are affected. Human vision is tolerant of considerable variation in lighting, apparently using the periphery of the viewing field to normalize the color interpretation, or by assuming known colors for some recognized objects.

In the context of processing images in frequency space, kernels can be analyzed efficiently in that domain to understand their smoothing properties. One of the very useful "shapes" for a weight kernel is that of a Gaussian. This is a set of weights that

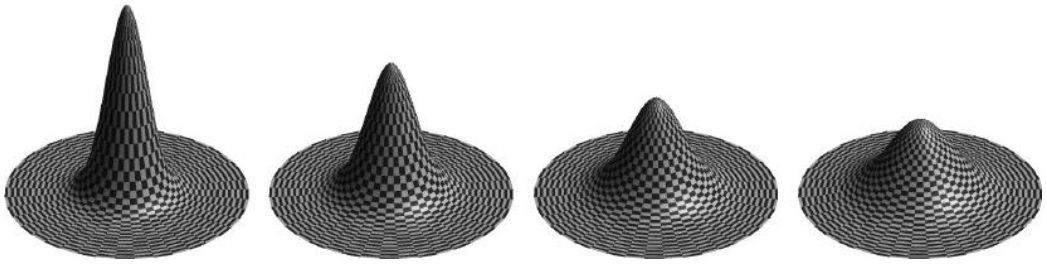

Figure 2.8: Graphical plot of the weight values in Gaussian smoothing kernels. As the standard deviation increases, the peak value drops so that the total sum of the weights (the volume under the plotted surface) remains constant [42].

approximates the profile of a Gaussian function along any row, column, or diagonal through the center. It is characterized by a standard deviation, expressed in terms of pixel dimensions, and calculated as:

$$G(x, y, \sigma) = \frac{1}{2\pi\sigma^2} \exp\left(-\frac{x^2 + y^2}{2\sigma^2}\right) \tag{2.2}$$

where x and y are the distance in pixels from the center of the kernel. The size of the kernel is 3 times the standard deviation on either side of the central pixel, so that adding another row of values would insert negligibly small numbers into the array. The standard deviation for these kernels is the radius (in pixels) containing 68% of the integrated magnitude of the coefficients, or the volume under the surface if the kernel is pictured as a 3D plot of the weight values, as shown in Fig. 2.8. This is a two-dimensional generalization of the usual definition of standard deviation; for a one-dimensional Gaussian distribution, 68% of the area under the curve lies within $\pm$ 1 standard deviation.

Gaussian filters or windows are sometimes implemented in terms of a parameter α and the window length M [46]. Here, $\alpha \equiv 1/\tilde{\sigma}$ where $\tilde{\sigma} \equiv 2\sigma/(M-1)$, so that the window shape is invariant with respect to window length M.

Multiplication of the frequency transform by a convolution function is equivalent to application of a kernel in the spatial domain. The most common noise-filtering method is to remove high frequency information, which represents pixel-to-pixel variations associated with random noise. Such removal may be done by applying a filter or mask to reduce or eliminate higher frequencies, and retransforming. The result is the same as that which can be accomplished in the spatial domain.

In Section 2.2.4 on image enhancement, the use of kernels in which a ring of negative weight values surrounds a positive central peak is shown. The purpose of this modification is to sharpen edges and avoid some of the blurring that is produced by

smoothing out noise. The same method has long been used for the smoothing of one-dimensional signal profiles, such as X-ray diffraction patterns, spectra, or time-varying electronic signals. This is often performed using a fitting procedure [47].

2.2.3 Histogram equalization

In addition to standard mathematical functions, it is sometimes advantageous to construct a transfer function for a specific image. The goal is a specific algorithm that gives reproducible and (hopefully) optimal results. The most popular of these methods is histogram equalization [48]. To understand it, it is helpful to begin with the image brightness histogram.

The conventional histogram plot shows the number of pixels in the image having each of the 256 possible values of stored brightness (or, for images with a greater dynamic range, the number of pixels with brightness values that fit into 256 linear counting bins). Peaks in the histogram correspond to the more common brightness values, which may correspond to particular structures that are present. Valleys indicate brightness values that are less common in the image. The data can also be plotted as a cumulative curve, which is just the integral or summation of the values. If this curve is used as the display transfer function, the result is a display in which all of the available 256 brightness values are equally used. The histogram of this processed image shows this uniform distribution (hence the name histogram equalization) and a linear cumulative plot. (Since all pixels having the same initial brightness value are reassigned to the same new value, the histogram is only approximately flat.)

For a color image, it is possible to show three histograms corresponding to the three color axes or channels. As shown in Fig. 2.9b, this can be done for RGB, HSV, or Luv color coordinates. Any of these sets of histograms fails to fully characterize the image, however, because they do not show the combinations of values that are associated in the same pixels. A three-dimensional histogram in which points in the histogram have coordinates that correspond to the color values showing the number of pixels with each combination of values is illustrated in Fig. 2.9c. Darker values indicate a greater number of pixels with a particular combination of channel values. The projections of the three-dimensional histogram onto each of the two-dimensional faces of the cube are shown. This approach is used in Section 2.2.5 in the context of selecting color combinations for thresholding.

Histogram equalization automatically determines a transformation function that seeks to produce an output image that has a uniform histogram. There are applications in which attempting to base enhancement on a uniform histogram is not the best approach. In particular, it is useful sometimes to be able to specify the shape of the

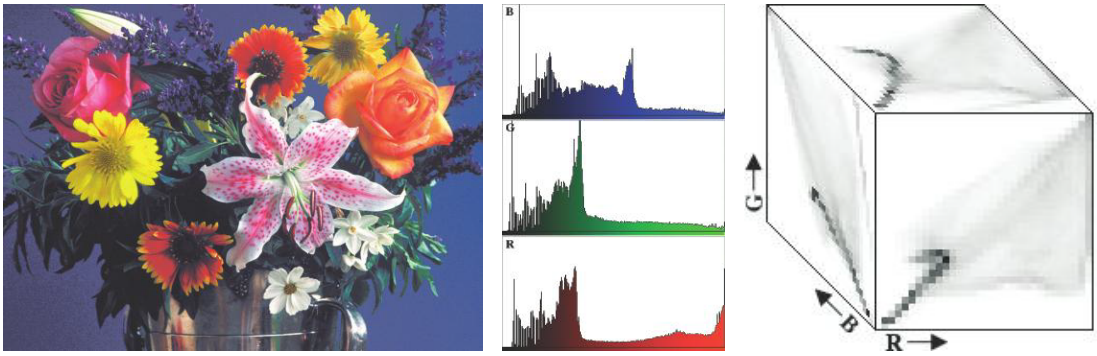

(a) **(b)** **(c)**

Figure 2.9: Histograms of channels in a color image. (a) Image. (b) RGB histogram. (c) RGB three-way histogram [42].

histogram that the processed image is wished to have. The method used to generate a processed image that has a specified histogram is called histogram matching or histogram specification [49].

Local equalization of image contrast produces an increase in local contrast at boundaries. This has the effect of making edges easier for the viewer to see, consequently making the boundaries appear sharper (although the increased noise within the nearly uniform regions may offset this improvement). There are several other approaches to edge enhancement that are less sensitive to overall brightness levels, noise, and the type or scale of detail present than the equalization discussed above. A very simple kernel that is still roughly symmetrical, but does not have exclusively positive values, is the classic 3×3 Laplacian operator:

$$\begin{bmatrix} -1 & -1 & -1 \\ -1 & +8 & -1 \\ -1 & -1 & -1 \end{bmatrix} \tag{2.3}$$

This subtracts the brightness values of each of the eight neighboring pixels from eight times the central pixel. Consequently, in a region of the image that is uniform in brightness or has a uniform gradient of brightness, the result of applying this kernel is to reduce the value to zero. When a variation is present within the neighborhood in the form of a point, line, or edge, the result of the Laplacian is a non-zero value. It may be either positive or negative, depending on where the central point lies with respect to edge, etc.

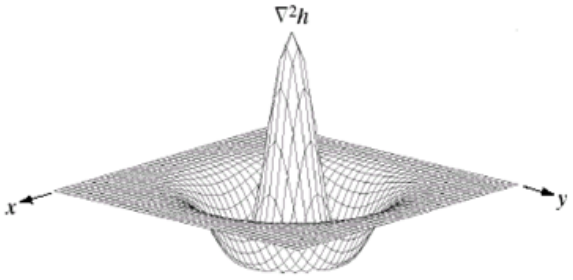

Figure 2.10: Graphical plot of the weight values in Laplacian of Gaussian kernels. Standard deviation determines zero-crossing of the inner body. The sum (or average) of all elements of the kernel has to be zero so that the convolution result of a homogeneous regions is always zero [49].

2.2.4 Edge detection

As the name of the Laplacian operator implies, it is an approximation to the second order differential operator of brightness B in directions x and y:

$$\nabla^2 \equiv \frac{\partial^2 B}{\partial x^2} + \frac{\partial^2 B}{\partial y^2} \tag{2.4}$$

which is invariant to rotation, and hence insensitive to the direction in which the discontinuity runs. This highlights the points, lines, and edges in the image and suppresses uniform and smoothly varying regions. By itself, this Laplacian image loses information about the overall shape of the subject. Adding the Laplacian enhancement of the edges to the original image restores the overall gray scale variation which the human viewer can comfortably interpret. It also sharpens the image by locally increasing the contrast at discontinuities. This can be done by changing the weights in the kernel, so the +8 element in 2.3 becomes +9.

Closely related to unsharp masking, the most general form of this technique is the subtraction of one smoothed version of the image from another having a different degree of smoothing. This is called the Difference of Gaussians (DoG) method and is believed to be similar to the way the human visual system locates boundaries and other features [50]. The DoG is practically identical in shape to another function that is also used, the Laplacian of a Gaussian, or LoG (also known as a Marr–Hildreth operator).

An appropriate filter for intensity changes detection is found to be the second derivative of a Gaussian, and it is shown that, provided some simple conditions are satisfied, these primary filters need not be orientation-dependent [51]. LoG as an operator or

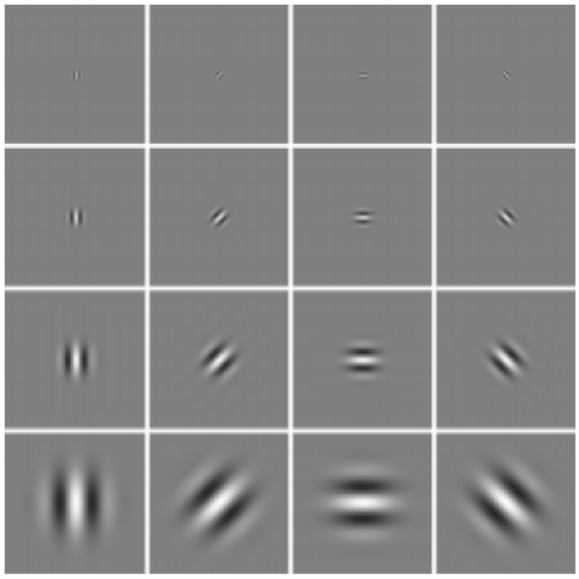

Figure 2.11: Real part of the 4×4 Gabor functions in the spatial domain. Horizontal orientation variation can easily be seen, as well as incremental sinusoid wavelength and Gaussian standard deviation (blob radius) from top to bottom [52].

convolution kernel is defined as in (2.5), where σ is Gaussian standard deviation. This operator is also known as Mexican hat because of its shape (Fig. 2.10).

$$LoG \equiv \frac{\partial^2}{\partial x^2} G_\sigma(x,y) + \frac{\partial^2}{\partial y^2} G_\sigma(x,y) = \frac{x^2+y^2-2\sigma^2}{\sigma^4} e^{-(x^2+y^2)/2\sigma^2} \tag{2.5}$$

Another useful filter is the Gabor filter. It is the product of a 2-D Gaussian function and a complex exponential function. Its shape can vary according to the parameters in (2.6), as in Fig 2.11.

$$g_{\theta,\lambda,\sigma}(x,y) = \exp\left\{-\frac{x^2+y^2}{2\sigma^2}\right\} \exp\left\{\frac{j\pi}{\lambda}(x\cos\theta + y\sin\theta)\right\} \tag{2.6}$$

2.2.5 Multiband images segmentation

In some cases, segmentation can be performed using multiple images of the same scene. The most familiar example is that of color imaging, which uses different wavelengths of light.

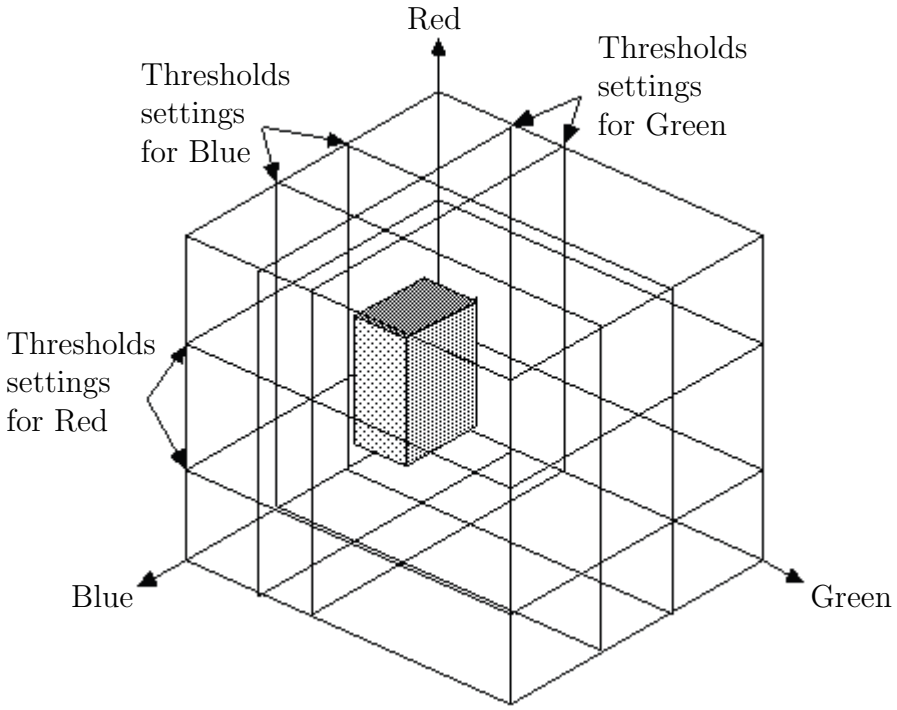

Figure 2.12: Illustration of the combination of separate thresholds on individual color channels. The shaded area is the AND of the three threshold settings for red, green, and blue. The only shape that can be formed in the three-dimensional space is a rectangular prism. [42].

In general, the more independent color bands or other images that are available, the better the job of segmentation that can be performed. Points that are indistinguishable in one image may be fully distinct in another. However, with multi-spectral or multi-layer images, it can be difficult to specify the selection criteria. The logical extension of thresholding is to place brightness thresholds on each image, for instance to specify the range of red, green, and blue intensities (or L, u and v). These multiple criteria are then usually combined with an AND operation (i.e., the pixel is defined as part of the foreground if its three RGB components all lie within the selected ranges). This is logically equivalent to segmenting each image channel individually, creating separate binary images, and then combining them with a Boolean AND operation afterward. It is also equivalent to segmented hexahedra as Cartesian products of channel intervals.

Using three one-dimensional histograms and sets of threshold levels, for instance in the RGB or Luv case, and combining the three criteria with a logical AND selects pixels that lie within a portion of the color space that is a simple prism, as shown in Fig. 2.12. If the actual distribution of color values has some other shape in the color

space, for instance if it is elongated in a direction not parallel to one axis, then this simple rectangular prism may be inadequate to select the desired range of colors.

2.3 Pattern Recognition and Classification

Once images and their information are processed, understanding and automatically integrating clinical procedures, recognition and classification decisions must be made. Machine learning is performed by certain methods, especially when a training phase is required for detection and localization purposes in development chapter. Statistical concepts are also necessary for performance evaluation throughout the process.

2.3.1 k-nearest neighbor regression

Given an unknown feature vector x and a distance measure, then:

- Out of the N training vectors, identify the k nearest neighbors (kNN), irrespective of class label. k is chosen to be odd for a two class problem, and in general not to be a multiple of the number of classes M.
- Out of these k samples, identify the number of vectors. k_i, that belong to class ω_i, $i = 1, 2, \ldots, M$. Obviously, $\sum_i k_i = k$ [53].

The regression case [54] varies in a simpler way. Having a training set with pairs of measurements (d, x), d for a new measurement needs to be estimated by knowing just x. x in training and test sets are vectors in a multidimensional feature space [55]. Estimation is made by computing the distance (in the feature space) between the new feature vector and the ones in the training set. Various distance measures can be used, including the Euclidean and Mahalanobis distance, and the k smaller ones are chosen. The value (d) is simply assigned to the average of the values of its kNN (Fig. 2.13).

k is chosen according to the problem, its results and computational complexity. Resulting d can also be computed by weighting the contributions of the neighbors according to their distance.

A serious drawback associated with kNN techniques is the complexity in search of the nearest neighbor(s) among the N available training samples [53]. Brute-force searching amounts to operations proportional to $kN(O(kN))^2$. The problem becomes particularly severe in high-dimensional feature spaces. To reduce the computational burden a number of efficient searching schemes have been suggested [56–58].

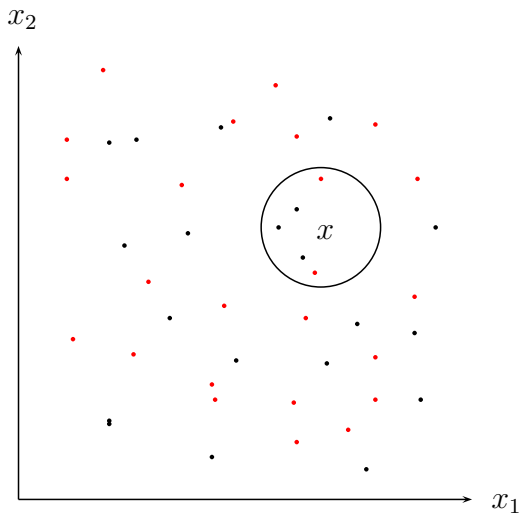

Figure 2.13: The k-nearest neighbor query starts at the test point and grows a spherical region until it encloses k training samples, and labels the test point by a majority vote of these samples. In this $k = 5$, two-dimensional binary case, the test point x would be labeled the category of the black points [55].

This method is applied for pixel-level position regression in Section 3.3.

2.3.2 Fuzzy c-means

Fuzzy c-means (FCM) is a method of clustering which allows one piece of data to belong to two or more clusters [59, 60]. This method is based on minimization of the following objective function:

$$J_{FCM}(U, v; X) = \sum_{k=1}^{n} \sum_{i=1}^{C} (\mu_{ik})^m \|x_k - v_i\|^2, \qquad 1 \leq m < \infty \tag{2.7}$$

where m is any real number greater than 1, μ_{ik} is the degree of membership of x_k in the cluster j, x_k is the ith of d-dimensional measured data, v_i is the d-dimension center of the cluster, and $\|\cdot\|$ is any norm expressing the similarity between any measured data and the center.

Fuzzy partitioning is carried out through an iterative optimization of the objective function shown above, with the update of membership μ_{ik} and the cluster centers

$$\mu_{ik} = \frac{1}{\sum_{j=1}^{C} (\|x_k - v_i\| / \|x_k - v_j\|)^{2/(m-1)}}, \qquad v_i = \frac{\sum_{k=1}^{n} (\mu_{ik})^m x_k}{\sum_{k=1}^{n} (\mu_{ik})^m} \tag{2.8}$$

This iteration will stop when $max_{ik}\{|\mu_{ik}^{(n+1)} - \mu_{ik}^{(n)}|\} < \varepsilon$, where ε is a termination criterion between 0 and 1, whereas n are the iteration steps. This procedure converges to a local minimum or a saddle point of J_m.

This method is applied for pixel-level image segmentation in Section 3.4.

2.3.3 Artificial neural networks

In a practical application of discriminant functions, specific parameterized functional forms are chosen, and the values of the parameters are then determined from a set of training data by means of a suitable learning algorithm. The simplest choice of discriminant function consists of a linear combination of the input variables, in which the coefficients in the linear combination are the parameters of the model, and has been considered widely in the literature on conventional approaches to pattern recognition. This simple discriminant can be generalized by transforming the linear combination with a non-linear function (called an activation function) which leads to concepts such as logistic regression and the perceptron. Another extension involves transforming the input variables with fixed non-linear functions before forming the linear combination, to give generalized linear discriminants. These various forms of linear discriminant can be regarded as forms of neural network in which there are single or multiple layers of adaptive weights between the inputs and the outputs [61].

Representational capabilities of multilayered networks (Fig. 2.14) have either threshold or sigmoidal activation functions. Such networks are generally called multi-layer perceptrons, even when the activation functions are sigmoidal. For networks having differentiable activation functions, there exists a powerful and computationally efficient method, called error backpropagation, for finding the derivatives of an error function with respect to the weights and biases in the network [61].

Backpropagation is one of the simplest and most general methods for supervised training of multilayer neural networks. Other methods may be faster or have other desirable properties, but few are more instructive. It is a straightforward matter to find how the output (and thus error) depends on the hidden-to-output layer weights [55].

If the "proper" outputs for a hidden unit were known for any pattern, the input-to-hidden weights could be adjusted to approximate it. However, there is no explicit teacher to state what the hidden unit's output should be. This is called the credit assignment problem. The power of backpropagation is that it allows us to calculate an effective error for each hidden unit, and thus derive a learning rule for the input-to-hidden weights [55].

Networks have two primary modes of operation: feedforward and learning. Feedfor-

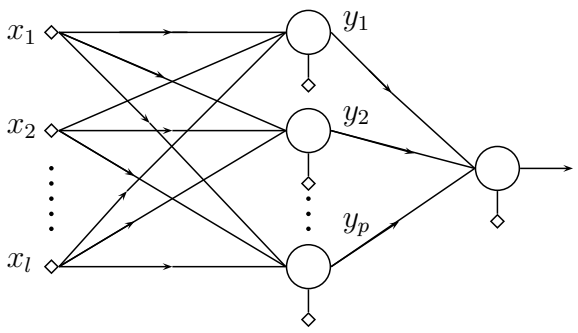

Figure 2.14: A two-layer perceptron. Input vectors are in the l-dimensional space ($x \in \mathbb{R}^l$), p neurons are in the hidden layer and there is one output neuron [53].

ward operation, consists of presenting a pattern to the input units and passing the signals through the network in order to yield outputs from the output units. Supervised learning consists of presenting an input pattern as well as a desired, teaching or target pattern to the output layer and changing the network parameters (e.g., weights) in order to make the actual output more similar to the target one [55].

This method is applied for region-level classification in Section 3.4.

2.4 Performance indicators

In order to quantify massive results, standard statistical measures must be defined. Counting on expert ground-truth parameters, disease can be present or absent. Specifically, abnormality that reveals the condition can appear or not. On the other hand, test outcome (classification result) can be positive or negative. Relationships between these are clarified in Table 2.3.

The main indicators for this matter are sensitivity and specificity. They can be obtained from true positives (TP), false positives (FP) —or type I error—, false

Table 2.3: Relationships among evaluation terms

	Condition Positive	Condition Negative
Test Outcome Positive	True Positive	False Positive
Test Outcome Negative	False Negative	True Negative

negatives (FN) —or type II error— and true negatives (TN). Sensitivity is the rate of correctly diagnosed abnormal samples among the actual abnormal samples, while specificity is the ratio between correctly detected normal cases among actual normal cases, as in (2.9). Therefore, reaching a value of 1 (100%) is the goal for both of them.

$$\begin{aligned} \textit{Sensitivity} &= \frac{TP}{TP+FN} \\ \textit{Specificity} &= \frac{TN}{TN+FP} \end{aligned} \tag{2.9}$$

Not so commonly used in this work, but worth mentioning, are precision and accuracy. This indicators allow overall performance evaluation and may not be as clinically relevant as previous ones. (2.10) shows how to calculate them.

$$\begin{aligned} \textit{Precision} &= \frac{TP}{TP+FP} \\ \textit{Accuracy} &= \frac{TP+TN}{TP+FP+FN+TN} \end{aligned} \tag{2.10}$$

Furthermore, sensitivity and specificity are the evaluation criteria of this work results. For the system as a whole and for each of its specific detection stages, these indicators note how well the performance is. They lead directly to numbers in released specialist capacity and resources, as well as misdiagnosed patients.

It is important to keep in mind that for this work, as for any medical purpose, sensitivity is much more important and delicate than specificity. Assuming 100 patients, each percentage point less in sensitivity results in an ill patient sent away from treatment until next scheduled checkup.

In the other hand, one point less in specificity only means a healthy patient sent to the specialist. Moreover, although not involving medical risk, this undermines health system capacity release and improvement in specialists allocation.

This topic also influences directly in objectives of design. Several intermediate steps in detection stages demand threshold selection, balancing between sensitivity and specificity achievement. As has been said, there should be a fair balance between both of them, but always holding the first one at a high rate. This ensures keeping a low leakage of patients affected by the disease.

Finally, in contrast to the above concept, the higher the specificity rate, the more efficient the system. So, therefore, more profitable and attractive if you are looking to optimize resource allocation.

2.5 State of the Art

A general revision of previously accomplished work needs to be made for two major purposes: (1) develop this work building on best available results and (2) orient and locate the reader in the current research and application context. This section goes through very similar parts to those in development chapter; this is because research has been conducted independently in these four major themes. An additional fifth matter is briefly described because of its similarity with this very application of concepts.

Each of the four following tables are arranged in a similar way. For each research theme, main publications are sorted by year of appearance. Feasibility refers to a somewhat ambiguous term: evaluation of the complexity, degree of depth of methods' description and implementation time demand (taking into account this work's time resources). The paper marked with an asterisk denotes the selected approach for each of the stages development. The amount of works citing each author is as of fourth quarter of 2011 through first quarter of 2012. Some of the data was not available (N/A) at the time.

For blood vessel localization, different investigations in the past have taken place. Evaluation of existing methods on a common database of screening images has been performed [62], detection has been based on the regional recursive hierarchical decomposition using Quadtrees and post-filtration of edges [63], Gabor wavelet transform responses taken at multiple scales with Gaussian mixtures classifier [64] and combination of shock filter and Binarization [65]. Table 2.4 summarizes this literature. Performance item is omitted because of its variability between authors and its high relativity to experts ground-truth parameters reliance.

OD localization has been proposed by (Table 2.5) the combination a Hausdorff-based template matching technique on edge map, guided by a pyramidal decomposition for large scale object tracking [66], model parameters identified by means of a simulated annealing optimization technique [67], fitting a single point-distribution-model to the image, that contains points on each structure, using a cost function, which is based on a combination of both global and local cues [68], matching the expected directional pattern of the retinal blood vessels [69] and prediction of the distance to the object of interest at any given location based on a set of features measured at that location, using a kNN regressor [70]. Fovea localization is not covered because it is not implemented in this approach.

Bright lesions have been found using their high grey level variation, and their contours are determined by means of morphological reconstruction techniques [71], retinal pixel and lesion classification using kNN and linear discriminant classifiers [72], fuzzy mor-

phology for lesion enhancement [73], fuzzy c-means segmentation, classified using a multilayer neural network classifier [74] and contextual information incorporation [75] (Table 2.6).

For red lesions detection, Table 2.7 sums up application of a region-of-interest and matched-filter use [76], enhancement of small round features after removal of variations in background intensity [77], scale and orientation selective Gabor filter banks usage [78], vasculature and red lesions separation from the background of the image, using a set of features and a kNN classifier [79] and investigation of a set of optimally adjusted morphological operators [80], surveyed approaches for red lesions detection.

Overall DR detection system has also been evaluated before. One of the main exponents [12] performed limited tasks including: localization of the OD, segmentation of retinal vessels, detection of red and bright lesions, plus discarding of images with insufficient image quality [14]. Results were a sensitivity of 0.84 and a specificity of 0.64. The other publication [13] performed sensitivity and specificity of 0.839 and 0.727, respectively. To conclude, they determined automated detection of DR using published algorithms cannot yet be recommended for clinical practice, yet they are a reliable alternative to time-consuming manual analysis as computer-aided diagnosis algorithms.

According to the mentioned concepts (year of publication, performance, feasibility and number of other publications citing them), one approach is selected for each stage. The more recent the publications, the more likely they are to incorporate prior knowledge and correct problems presented when starting research on the subject. Of course, performance is the most relevant feature of all. However, it is expected that, although the approach is to be implemented literally, the results will not be the same. This is because a local database of images will be used for this work, and not the standardized and adjusted, publicly available ones. Feasibility concept ensures, on one hand, the possibility to effectively implement the method and, secondly, to do so in the intended time for this phase of the project. The number of authors who cite the publication is related to its credibility and usefulness.

Approaches that meet all the above features are chosen for their development and implementation. In this way, it is expected to build a comprehensive system that yields results of detection of DR as a whole, justifying each of its manifestations. The results should be comparable with the overall DR detection systems described above.

Table 2.4: Blood vessels localization state of the art

Author	Year	Feasibility	Cited by
Niemeijer et al. [62]	2004	Medium	195
Dua et al. [63]	2005	Medium	12
*Soares et al. [64]	2006	High	175
Kumar et al. [65]	2009	Medium	N/A

Table 2.5: Optic disc localization state of the art. Performance means precision and precision in normal/abnormal images when applies

Author	Year	Performance	Feasibility	Cited by
Lalonde et al. [66]	2001	.9300	Medium	115
Foracchia et al. [67]	2004	.9800	High	126
Niemeijer et al. [68]	2006	.984/.94	Medium	59
Abdel et al. [69]	2008	.9877	High	59
*Niemeijer et al. [70]	2009	.994/.93	High	19

Table 2.6: Bright lesions detection state of the art. Performance means sensitivity/specificity

Author	Year	Performance	Feasibility	Cited by
Walter et al. [71]	2002	.928/.924	High	180
Niemeijer et al. [72]	2007	.95/.88	Medium	53
Mansoor et al. [73]	2008	N/A	High	1
*Osareh et al. [74]	2009	.935/.921	High	12
Sanchez et al. [75]	2010	N/A	Medium	4

Table 2.7: Red lesions detection state of the art. Performance means sensitivity/specificity

Author	Year	Performance	Feasibility	Cited by
Cree et al. [76]	1996	.82/.84	Low	21
Hipwell et al. [77]	2000	.85/.76	Low	67
Vallabha et al. [78]	2004	N/A	Low	16
Niemeijer et al. [79]	2005	1.0/.87	Medium	99
*Sopharak et al. [80]	2011	.8161/.9999	Medium	31

Chapter 3

Design and Implementation

In this chapter every step of the design and implementation is described in detail. First of all, design in terms of stages order is exposed. Then, data base general construction, necessary equipment and expert knowledge integration are explained. Finally, each processing stage is fully described.

As has been said, the objective is to develop a system for automated DR detection. The input of the system is a digital image corresponding to a retinal exam. All images were clinically validated as appropiate for DR diagnosis. DR presence results from any of two type of abnormalities presence: bright lesions or red lesions. Therefore, both types of lesions should be looked for in the image. Besides methods specific to the type of search, morphological landmarks of any retina (OD and blood vessels) need to be located as well because of their graphical structure reliance when looking for abnormalities.

Fig. 3.1 shows a very simplified diagram of DR detection proposed method, including processing and classification intermediate steps. Bright and red lesions detection could be seen as a parallel process; however, it is noted that the first one is necessary as an intermediate step of the second.

Selected approaches for each step of detection, disclosed extensively throughout this chapter, need completeness of one another. For bright lesions detection, OD must be located. For OD localization, blood vessels must be segmented. Now, for red lesions detection, pixels of the image corresponding to bright lesions, blood vessels and OD are discarded in order to analyze the background of the retina for additional abnormalities.

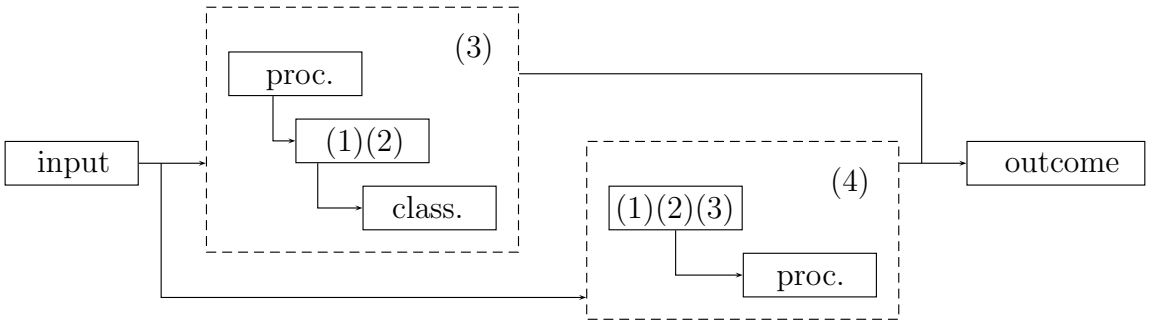

Figure 3.1: DR detection presented approach. Input is digital retinal image, outcome is DR presence/absence. (1) Blood vessel segmentation, (2) OD localization, (3) bright lesions detection and (4) red lesions detection. When in solid box, stage numbers mean required condition for corresponding pixels extraction.

3.1 Materials

A dataset 500 of images for training and testing purposes was obtained from a DR screening program of CRS center. This images were acquired using a Canon CR DGi nonmydriatic retinal camera (EOS 30D). JPEG image compression was applied. Images were resized to 701×468 pixels because of state of the art experiences. Images are non-stereoscopic pictures of $45°$, ones with macular field and another ones with disc/nasal field [38]. The system was implemented using MATLAB software.

Experts were ophthalmologists from *Universidad de Chile*. They labeled images into lesion and nonlesion, as well as OD and fovea centers locations. For this matter, a specially designed graphical user interface (GUI) was designed (Fig. 3.2). For bright lesions detection, a pixel-level precision detection is not critical. Therefore, a post-segmentation method is used to validate the training and testing databases. This is, a 500 image database is previously segmented using the section listed algorithms is handed to medical specialists, in addition to an ad-hoc graphical user interface.

Accessing one image at a time, the regions coordinates are also loaded into the system. The user runs through the different regions (clustered in the retinal image segmentation stage), which are automatically marked with enough contrast. This allows him to acknowledge if the region of interest is a bright lesion or not. A checkbox lets him mark and unmark the region in case of doubts. It is mandatory to classify the whole region set of the image in order to save and proceed.

In addition to region labeling, a module for OD and fovea centers is provided. The first one has as much as priority restriction as region labels, while the second tag is

Figure 3.2: Labeling GUI. Studied image on the left and buttons panel (region switching and labeling, OD and fovea marking) on the right. Blue pixels mark region of interest, which must be labeled as bright lesions or not (omitting OD pixels).

optional. This is consistent with the existence of different angles of retina captured by the digital images, causing aleatory presence of the macular area and, therefore, the fovea. These tags (specially OD center) are used to train and test OD localization algorithms in order to mask it and perform feature extraction.

Training and testing sets are specified in the corresponding section, because they differ according to expert labeling. Red lesions detection does not need a training set.

3.2 Blood Vessels Localization

Retinal blood vessels segmentation from the rest of the image components is mandatory in orer to detect DR related abnormalities. In this case, it is necessary for OD localization and for red lesions detection. In this work, methods are not fully developed and therefore not deeply explained. This is because, as it is an intermediate step in DR detection, available open source scripts for implementation has been used.

The implemented method [64] produces segmentations by classifying each image pixel as vessel or nonvessel, based on the pixel's feature vector. Feature vectors are composed of the pixel's intensity and two-dimensional Gabor wavelet transform responses

(a) (b) (c)

Figure 3.3: Vessels segmentation intermediate results produced by the GMM classifier. (a) Original image. (b) Posterior probabilities. (c) Segmentation.

taken at multiple scales. The Gabor wavelet is capable of tuning to specific frequencies, thus allowing noise filtering and vessel enhancement in a single step. A Bayesian classifier with class-conditional probability density functions (likelihoods) described as Gaussian mixtures is used, yielding a fast classification, while being able to model complex decision surfaces. The probability distributions are estimated based on a training set of labeled pixels obtained from manual segmentations. Blood vessel localization stage is fully taken from the mentioned authors work.

Training phase is crucial for this approach. Manually segmented images need to be used for this stage to work. The DRIVE [81] database is used for this purpose; it consists of 40 images (seven of which present pathology), along with manual segmentations of the vessels. The images are captured in digital form from a Canon CR5 nonmydriatic 3CCD camera at 45° field of view (FOV). The images are of size 768×584 pixels, eight bits per color channel and have a FOV of approximately 540 pixels in diameter. The images are in compressed JPEG format. The images have been manually segmented by three observers trained by an ophthalmologist.

Besides preprocessing and further feature normalization, pixel features regarding wavelet transform features fine tuning is explained by certain parameters. This may result in differing results as it affects directly training guidelines. The 2-D Gabor wavelet was chosen for the purposes of this work, due to its directional selectiveness capability of detecting oriented features and fine tuning to specific frequencies [82,83]. This latter property is especially important in filtering out the background noise of the fundus images. The 2-D Gabor wavelet is defined as

$$\psi_G(x) = exp(jk_0x)exp\left(-\frac{1}{2}|Ax|^2\right) \tag{3.1}$$

where $A = diag[\epsilon^{-1/2}, 1]$, $\epsilon \geq 1$ is a 2×2 diagonal matrix that defines the anisotropy of the filter, i.e., its elongation in any desired direction. The Gabor wavelet is actually a complex exponential modulated Gaussian, where k_0 is a vector that defines the frequency of the complex exponential.

The ϵ parameter has been set to 4, making the filter elongated and $k_0 = [0, 3]$, i.e., a low-frequency complex exponential with few significant oscillations perpendicular to the large axis of the wavelet. These two characteristics are specially suited for the detection of directional features and have been chosen in order to enable the transform to present stronger responses for pixels associated with the blood vessels.

Moreover, the number of Gaussians modeling class-conditional probability density functions, k, is set to 20. Filtering is done using Gabor wavelet scales of 2 and 5. All of these, over the Gabor processed inverted green channel of each of the images.

With all this parameters in mind, five images from the DRIVE database and their corresponding segmentation maps are selected for training. This allows a working classifier to be constructed and further testing in any retinal digital image. The amount of images is not critical, but must be enough to ensure generalization and consider computational cost of training the classifier due to the large amount of possible samples.

Results are achieved using a Bayesian classifier in which each class-conditional probability density function (likelihood) is described as a linear combination of Gaussian functions [53, 55]; the Gaussian mixture model (GMM) classifier. Hence, an intermediate result of the method is the intensity image of posterior probabilities, where a segmentation threshold of 0.5 is used in order to obtain a binary result, as in Fig. 3.3.

A close look at Fig. 3.3 example reveals some pixels wrongly segmented as vessels, as well as the opposite. Reasons go from camera lens flaws to red lesions. This is absolutely not critical for OD localization, as vascular arch features are not majorly affected. Nevertheless, red lesions detection may suffer the consequences. Action is taken, and explained in Section 3.5, to handle this issue.

3.3 Optic Disc Localization

OD, together with the vasculature and the fovea, is one of the most important anatomical landmarks presented in retinal exams. Locating it is very useful for reference purposes, but most important is its relationship with abnormalities. In an automated system, it could be confounded with bright lesions because of their color similarity. Thus, the importance of its localization and masking.

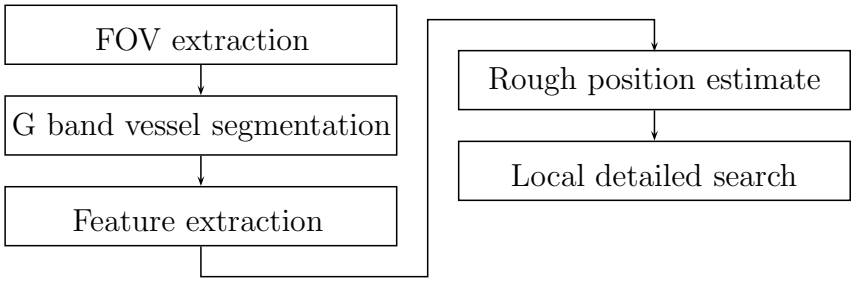

Figure 3.4: OD localization method. Second step is already processed from previous section. Final step is a repetition of the search process in a dense, specific area of the image.

A fast detection of the OD (with extension to fovea) is selected to develop this stage [70]. It makes few assumptions about the location of the structure in the image. The problem is defined as a regression problem. The distance is predicted in pixels in the image to the object of interest at any given location in the image based on a set of features measured at that location, using a kNN regressor. General layout of steps taken in this stage is shown in Fig. 3.4. Except for specific properly indicated steps, this stage is literally implemented from referenced authors.

Features combine cues measured directly in the image with cues derived from previous segmentation of the retinal vasculature. A distance prediction is made for a limited number of image locations and the point with the lowest predicted distance to the OD is selected as the OD center.

In this section 285 manually labeled images were used. 143 of them in the training phase (36 abnormal, 107 normal) and the method is evaluated in a separate dataset of 142 images (35 abnormal, 107 normal).

3.3.1 Position regression

The problem of locating anatomical structures in retina images is here defined as a regression problem. In regression, an empirical function is derived from a set of experimental data [84]. In general, regression analysis considers pairs of measurements (d, x) where variable x represents a set of measurements, the independent variables. The goal of regression is to find a function $f(\cdot)$ that can be used to predict the dependent variable d from x.

$$d = f(x, p) + \varepsilon \tag{3.2}$$

In (3.2) p is a parameter vector that controls the behavior of $f(\cdot)$ and ε is the error in the prediction of d by $f(\cdot)$. Naturally one would like to choose parameter vector p

so as to minimize ε. The problem of finding a certain location l in an image can be formulated as a regression problem [85] by taking the distance in the image to l as the dependent variable d and taking an image derived measurement as the independent variable x. The regression function can then be determined using a set of examples for which the distance to l, d as well as x are known. To find l in a new image, one only needs to find the location in which the estimated distance to l in that image is minimal.

A kNN regressor [54] is proposed as it performed well in preliminary experiments and allows straightforward feature selection. The regression function $f(\cdot)$, in this case parameter vector p only contains a single parameter, k, the number of neighbors. The kNN regressor requires a training phase in which measurement pairs (d, x) that are collected from various locations in a set of training images are put together in a training set. The measurement vectors in the training set x span a higher dimensional space, the feature space [55]. The estimated value of the dependent variable, $\hat{d}$, for an independent variable y measured somewhere in an image is determined by the values of d associated with the kNN in the feature space of y in the training set. By taking the average value of d amongst the kNN, $\hat{d}$ is determined.

3.3.2 Preprocessing

Each of the images is preprocessed before the localization of the OD commences. The FOV of the corresponding camera has been previously manually segmented and stored. This narrows the area of the image to be processed in terms of OD search.

The presented OD localization method uses only the green plane of the color image. The most important prerequisite of the method is the availability of a vessel segmentation. The input for this purpose is the method described in Section 3.2, where each pixel in the image is assigned a posterior probability that the pixel is inside a vessel [64]. To obtain a binary vessel map a threshold should be applied. It should be chosen low enough to include some of the smaller vessels around the fovea in the binary vessel map; it is set to 0.5 by vessel segmentation authors.

3.3.3 Vessel analysis

The local orientation and width of the retinal vasculature provide important clues to the position on the retina. By novel methods, (thinning, orientation, width, ends) proposed objectives are achieved. After preprocessing, a binary vessel map is available. It is thinned [86] until only the centerlines of the vessels remain. All cross-over points and bifurcations are eliminated by removing those centerline pixels that have

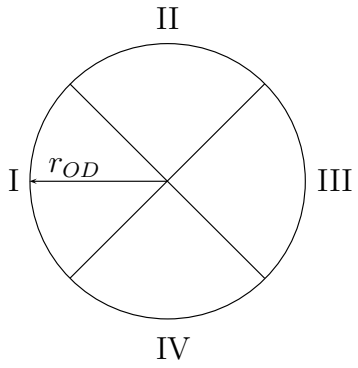

Figure 3.5: Template used to extract features for localization of the OD.

more than two neighbors. This is necessary because vessel orientation is not well defined in these points.

The orientation of the vessels is measured for each vessel centerline pixel by applying a 3×3 window centered on it and taking the angle (in radians ranging from $-\pi/2$ to $\pi/2$) between the x-axis and the major axis of the ellipse that has the same second-moments as the region. The window size is not a critical parameter, it was determined that this value gave adequate results in preliminary experiments. As it is not known in which direction the vessel flows, the local orientation α is expressed in radians where $\alpha \in [-\pi/2, \ldots, \pi/2]$.

The local vessel width w is measured for each centerline pixel on a line perpendicular to α. The distance from the centerline at which the binary vessel map indicates absence of vessel (edge). This is achieved using a line-drawing algorithm [87] where, instead of drawing pixel by pixel towards certain orientation, querying the continuity of the vessel. After the distance to the left and right edge of the vessel has been determined their sum to the centerline is taken as the local vessel width.

The ends of vessel segments can be near bifurcation points or vessel crossings and these can distort the vessel width measurements leading to a width overestimation. To compensate for this effect, w measurements over 20 pixels are replaced with the average of the width of their neighboring pixels in a 3×3 window, when they are below the conflictive measurement. The absolute vessel width is dependent on the number of degrees covered by the FOV and varies between subjects and in time due to the cardiac cycle. Therefore the measured w are normalized by dividing them by the maximum measured w in the image.

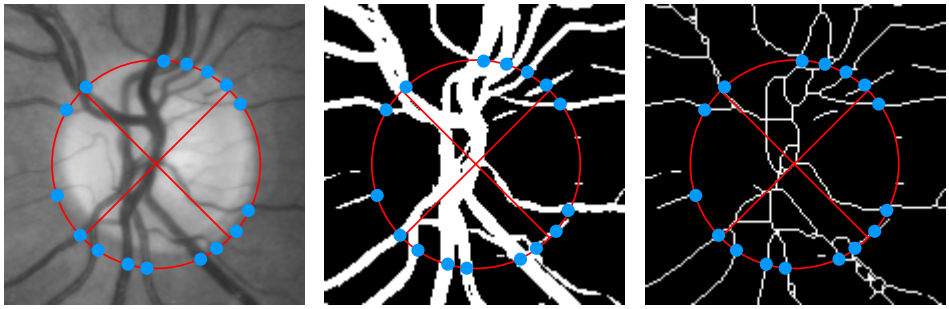

(a) (b) (c)

Figure 3.6: The OD template placed in a fundus image and two derived images. The points where unique vessel segments cross the template border are indicated by the blue dots. (a) The green plane of the color fundus photograph. (b) The vessel probability map. (c) The skeletonized vessel segmentation. The vessel centerline points that lie on the template border, marked by the dots, are the locations where the local vessel width and orientation based features are measured.

3.3.4 Template based feature extraction

There are many different independent variables (i.e. features) that can be measured in a retinal image and that may give information about the location in the image where one is measuring them. From the literature [69], two important cues that determine the location in the image emerge, image intensity based cues and vasculature based cues. Image intensity can be an important cue due to the fact that the OD in general is brighter than the surrounding retinal tissue. In this work, all image intensity based measurements are obtained in the green plane of the RGB retinal image. The pattern of the vasculature as it flows from and to the OD over the retina is similar in all images and the width of the vasculature changes as one moves further away from the OD. As such the local orientation and width of vessels provide important cues about the location in the image.

As OD is essentially a circular object, a set of features measured under and around a circular templates is proposed. Fig 3.5 shows the OD template. It consists of four quadrants and for each quadrant a set of features will be measured independently. The subdivision leads to more sensible features because one expects the vessels around the OD to have a specific orientation at the border of each of the four quadrants when the templates are placed on the OD in a retinal image. The template has a radius, r_{OD}, which is a free parameter that is dependent on the size of the image as well as the number of degrees of the retina shown in the FOV. As the number of degrees imaged in the FOV is unknown, some preliminary experiments were performed and

$r_{OD} = 50$ pixels was ser, roughly the radius of the object of interest in the training set after preprocessing.

The templates can now be used to extract features at a particular (x, y) location in the image. The template is centered on the location under consideration (see Fig. 3.6 for an example) and the set of features in Table 3.1 are measured for the OD template. In case the feature cannot be measured, e.g. because the template is partially outside the FOV or there are no vessels under the template, the feature values are set to 0. All the extracted features were normalized to zero mean and unit standard deviation.

The cues listed earlier in this section form the inspiration for the choice of this initial feature set. All features except 1 and 7 attempt to characterize the local vessel pattern. At the OD location one expects a large number (i.e. high density) of both very wide (i.e. the widest in the image) and narrow vessels that are flowing in a distinct direction which is different for every quadrant. The OD specific intensity features 1 and 7 simply characterize the local image intensity and standard deviation which are both expected to have a high value on top of the OD due to the bright appearance of the nerve tissue combined with the low intensity of the vessels.

A relatively large set of features has been initially defined (32). This complete set of features does not necessarily provide the best regression results. Application of a feature selection method improves overall system performance and decreases the computational complexity by reducing the dimensionality of the feature space. A supervised wrapper based feature selection method, Sequential Floating Feature Selection (SFFS) [88] was applied. The algorithm adds and removes features to and from the selected feature set when that improves the performance of the regressor.

Table 3.1: Set of features considered locate optic disc, decreasing in regression results importance

Feature	Description
1	Average image intensity under the complete template
2	Density of the vessels under the template
3–4	Number of vessels (quadrants IV, I)
5–6	Average difference in orientation (quadrants III, I)
7	Standard deviation of the image intensity under the complete template
8–10	Average width of the vessels (quadrant III, I, II)
11	Orientation of the vessel with the maximum width (quadrant III)
12	Average width of the vessels (quadrant IV)
13	Orientation of the vessel with the maximum width (quadrant I)
14–15	Average difference in orientation (quadrant IV, II)
16	Average vessel width under the complete template

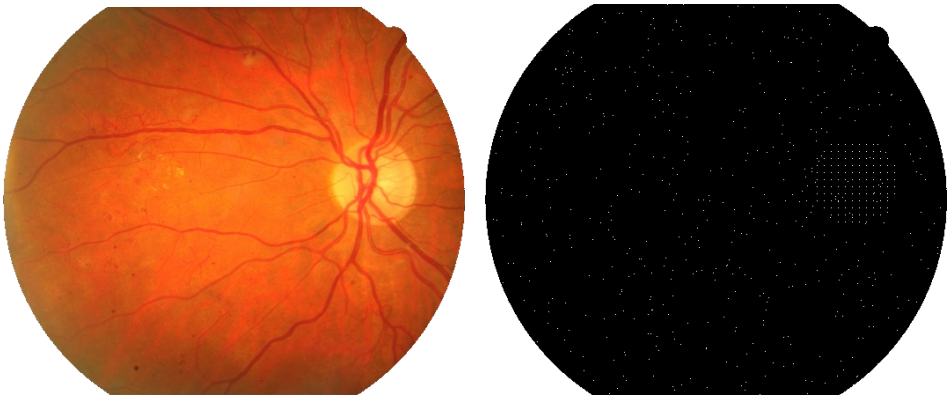

(a) (b)

Figure 3.7: OD training step feature extraction. (a) Original image. (b) Location of points where template was centered for feature extraction in the image. A more dense area can be seen around the OD location.

The performance in this case is measured by the average ε, the prediction error, over the dataset. This feature selection technique was applied to the OD training set by the authors, resulting in the mentioned 16 features choice.

3.3.5 Training phase

Before a regressor can be used to find a location in a previously unseen image, a one-time training phase needs to be completed. The training phase consists of the extraction of measurement pairs from a set of training images. To extract the measurement pairs from the 143 training images a two step sampling process was employed. In the first step the area around the known, correct object of interest within the radius of the template, r_{OD}, was sampled in a uniform grid spaced 8 pixels apart resulting in about 120 measurements per image. The spacing of the grid is not an important parameter as long as this area is sampled densely enough. For each of the sampled locations the appropriate template was used to extract all features which were stored in the training sample set together with the distance d to the true center of the object of interest.

In a second step a substantial number (500) of randomly selected locations (i.e. not on a grid) in the training image were sampled in a similar fashion. This resulted in a total of about 620 measurements per image. It is unlikely that the features measured around the template can provide accurate information for a robust estimation of d further away from the object of interest. Therefore, all samples obtained further than

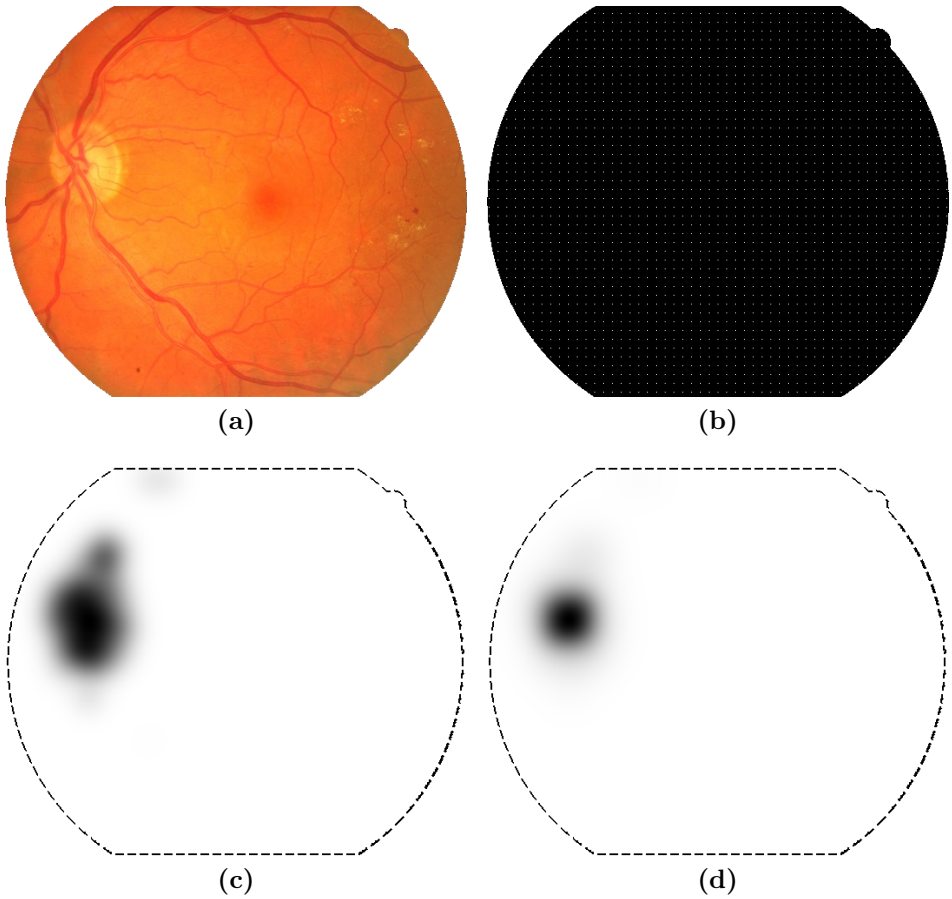

Figure 3.8: The OD detection step intermediate results. In the distance maps the border of the FOV is indicated by the dashed line. (a) Original image. (b) The 10×10 OD search grid, sampling points are represented by the bright pixels. (c) Blurred distance map, result of rough grid search for the OD center (lower intensity equals lower distance). (d) Blurred distance map of fine grid search for the OD center.

r away from the object of interest were assigned the value $d = r_{OD}$. An example of training feature sample extraction is shown in Fig. 3.7b.

Both k and the feature set have an influence on the regression performance. However, without assigning a value to k the wrapper based feature selection procedure cannot be performed. Therefore, authors of the original method determined an optimal $k = 21$ for the OD template.

3.3.6 Search strategy

No assumptions about the position of the OD in the retinal image are made. To locate it a two step search approach is used. First a rough estimate of the optic disc position is found followed by a more detailed search to refine the result. For $\hat{d}$ estimation, a kNN fast computing method [58] needs to be used to avoid one-by-one comparison computational complexity (customization of the original searching method).

The method starts by determining $\hat{d}$ for the OD for a set of pixels on a grid where the grid points are spaced 10 pixels apart in both the x and y direction and that is overlaid on top of the complete FOV of the retinal image (see Fig. 3.8b). The spacing of the grid is not a critical parameter, it should be dense enough so that there are sufficient responses near the OD center. Choosing a higher density of the grid leads to a greater computational complexity. For all pixels on the grid the value of $\hat{d}$ is determined and stored in a separate image, I_{result}. All pixels that are part of the FOV in I_{result} for which no $\hat{d}$ has been determined (i.e. that do not lie on the grid) are set to r_{OD}. To eliminate noisy estimates and determine the center of the OD I_{result} is then blurred using a large scale ($\sigma = 15$) Gaussian filter (see Fig. 3.8c). The scale of the Gaussian is not a critical parameter as long as it is sufficiently large. The rough location of the OD is found at the pixel location in I_{result} that has the lowest value. The search process is repeated with a 5×5 pixel grid centered on the rough OD location but constrained to a $r_{OD} \times r_{OD}$ search area (see Fig. 3.8d).

3.4 Bright Lesions Detection

Bright lesions and, specifically, exudates are one of the most important detectable retinal lesions. An automated method for screening purposes was selected and fully developed. This method is mostly inspired by a computational-based approach structure [74] with some changes and customization. Again, except for specific properly indicated steps, this stage is literally implemented from referenced authors.

Detecting retinal exudates in a large number of images that are generated by screening programmes and need to be repeated at least annually is very expensive in professional time and open to human error. With this motivation in mind, an efficient system to automate the preliminary analysis and diagnosis of DR disease is developed. This system combines computational intelligence and pattern recognition with machine learning techniques to analyze diabetic retinal images. Through this system, the abnormal (with DR presence) retinal images are automatically discriminated from normal images, and an accurate assessment of retinopathy severity is obtained at pixel level. Exudates, cotton wool spots, and drusen from color retinal images can

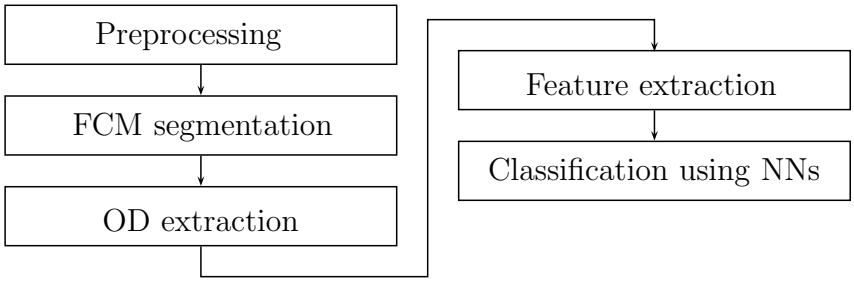

Figure 3.9: Bright lesions detection method. Preprocessing step includes histogram normalization and contrast enhancement, while segmentation includes coarse and fine stages. OD is excluded (through the results of previous section) from analyzed regions.

be discriminated by this method, but they will be equally considered, as they all represent abnormalities.

This method aims to investigate the effectiveness of computational intelligence toward automatic detection and identification of exudate pathologies. Starting with a color normalization and contrast-enhancement preprocessing steps, the retinal images are segmented based on a combination of color representation in Luv color space and an efficient coarse to fine segmentation using FCM clustering. To classify these regions into exudates and nonexudates, a neural network (NN) classifier is investigated. An explanatory diagram is shown in Fig. 3.9.

In this section 285 manually labeled images were used. 107 normal images and 36 abnormal images were used in the training phase, while 107 normal and 35 abnormal images were used in the evaluation phase.

3.4.1 Preprocessing

When looking at different patients' images from a database, one may immediately notice some major pigmentation differences between them. These differences may not be related to abnormalities. There are two main reasons for two images (usually from two different patients) to differ: color and contrast level of fundus. Thus, data goes through two preprocessing steps before commencing the detection of bright lesions.

A wide variation in the color of fundus from different patients is strongly correlated to the person's race, iris color and image acquisition lighting. Examples of this difference can be easily spotted in Fig. 3.11a–3.11d. To neutralize this effect, the first preprocessing step ensures each image is normalized in color terms [49].

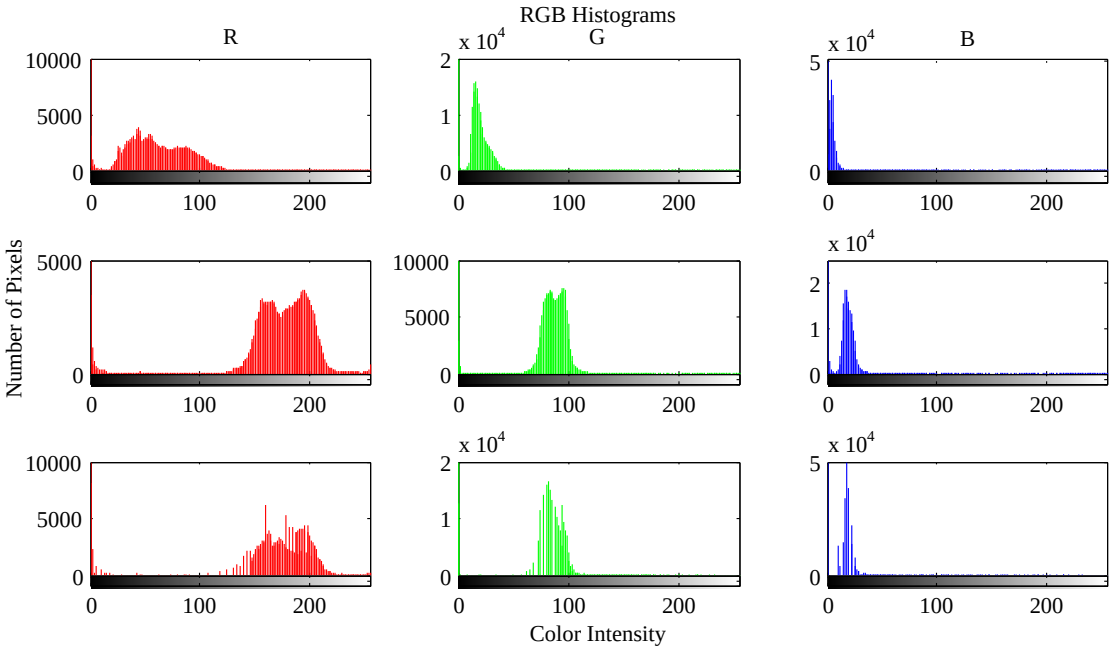

Figure 3.10: RGB histograms normalization. First row represents Fig. 3.11a three-way histogram, second row represents Fig. 3.11b three-way histogram and third one is the result of normalizing first to second (Fig. 3.11e). Number of pixels remains the same, but intensity relationship changes to the one in the reference image.

A retinal image is selected as reference (Fig. 3.11b) and its RGB color histogram is extracted. Then, a histogram specification is applied to modify the values of each image in the database [89] such that its frequency histogram matches the reference image distribution (Fig. 3.11e–3.11h).

The histogram specification technique was independently applied to each individual RGB channel to match the shapes of three specific histograms of the reference image (Fig. 3.10). Here, the reference histograms were taken from an image, which represents a frequent retinal pigmentation color among the image dataset.

The contrast of retinal images is not sufficient due to the intrinsic attributes of lesions and decreasing color saturation, especially in the periphery. Consequently, in the second preprocessing step, the contrast between the exudates and the retina background is enhanced to facilitate later segmentation. Local contrast enhancement [90] is applied to distribute the values of pixels around the local mean.

Before applying main algorithms, a previous transformation is required. The convenient color working space may not always be directly RGB. After a comparison between this one and HSI, the last one was demonstrated better for contrast issues [91].

In this sense, HSV model (value instead of intensity) is supported by MATLAB image processing toolbox and meets similar reasons of interest:

- The value and color information in the model are decoupled; the color content will not be affected by the application of the contrast enhancement technique to the value component and converting the result to RGB space for display on a visual display unit.

- Saturation and hue are closely related to the way we describe color perception.

This been said, value channel is extracted so local and global image information is taken into account. Some adjustments to the proposed routine has been made due to color space transformation; specifically, magnitude range of each pixel goes form 0 to 1, instead of 0 to 255.

While the contrast enhancement improves the contrast of bright lesions, it may also enhance the contrast of some nonlesion background pixels (e.g., noise), so that these pixels can wrongly be identified as bright lesions. Here, prior to contrast enhancement, a 3×3 median filter [92] is applied to suppress the noise.

A pixel p in the center of a small running window w is changed on each window step. The window's dimensions have been calculated balancing quality of the result and computation time; empirical outcome is a square window of side of approximately 12% of the whole original image side (length × width × 0.015). Window side must by an odd number (of pixels), so its center is changed to a new value p_n

$$p_n = \frac{[\phi_w(p) - \phi_w(\min)]}{[\phi_w(\max) - \phi_w(\min)]} \tag{3.3}$$

where

$$\phi_w(p) = \left[1 + \exp\left(\frac{\mu_w - p}{\sigma_w}\right)\right]^{-1} \tag{3.4}$$

and max and min are the maximum and minimum values in the whole image (chanel), while μ_w and σ_w indicate the local window mean and standard deviation, respectively. The exponential produces significant enhancement when the contrast is low (small σ_w), while it provides little enhancement if the contrast is high (large σ_w).

After the window finishes running through the whole image, resulting one must be transformed back to RGB space. Fig. 3.11i–3.11l shows the result of local contrast enhancement.

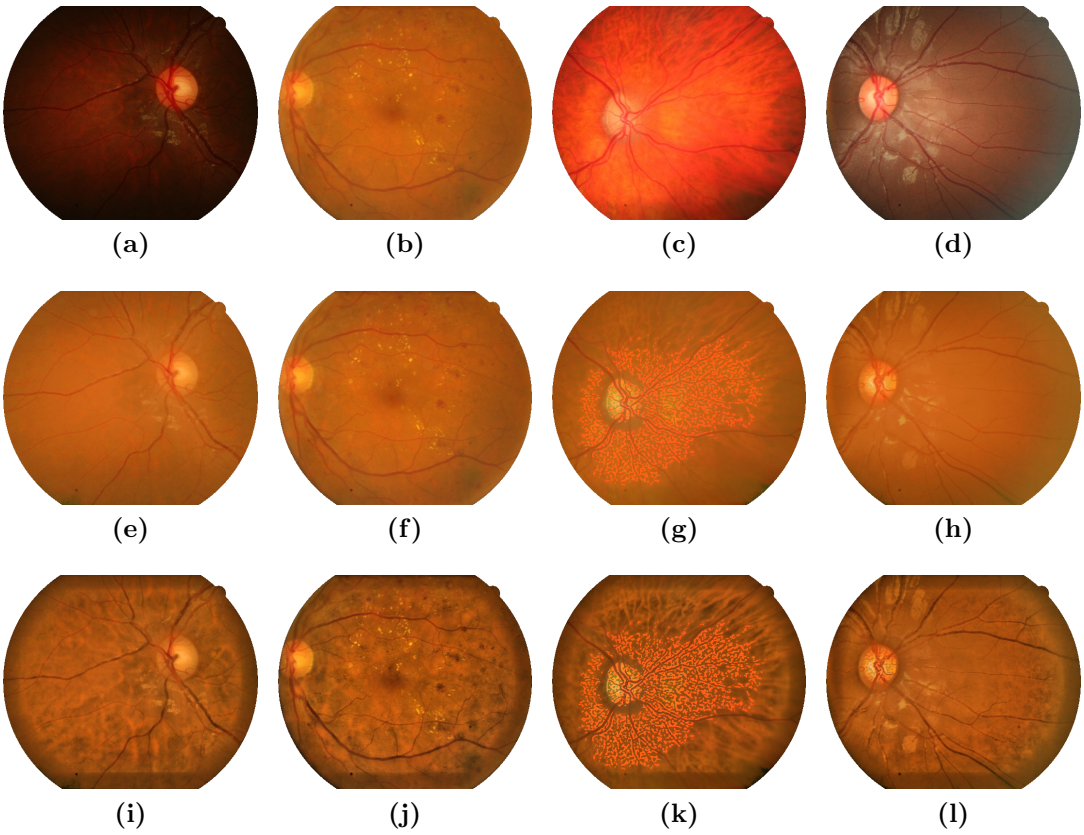

Figure 3.11: Typical color differences in fundus images, their normalization and contrast enhancement. Variance in terms of hue and contrast is very frequent and must be balanced to unify processing criteria; (b) Is the color reference image. (a), (c), (d) become (e), (g), (h) respectively. Contrast enhancement is applied to every example, resulting in (i)–(l).

3.4.2 Retinal image segmentation

Among various segmentation techniques, such as hard or fuzzy approaches, specificity for particular applications is taken into account for better performance. A two-stage color segmentation algorithm based on Gaussian-smoothed histogram analysis and FCMs clustering is used [93].

As it has been done before in this work, an appropriate representation using a color space definition is chosen. In a suitable color space, color pixels of interest can be clustered into well-defined, less overlapping groups, which are easily bounded by segmentation algorithms in the color space. Among spaces such as RGB, YIQ, HIS, HSL, Lab and Luv, the last one was found the most appropriate for this segmentation [74].

Hence, transformation to Luv space is the first thing that needs to be done.

3.4.2.1 Coarse segmentation

At the coarse stage, the segmentation algorithm utilizes the histogram information of the three 1-D color components to estimate the number of valid classes by a statistical evaluation of the histograms. It has been identified [94] that the derivatives, the extrema, and the interval bounded by the extrema of a histogram are useful information when carrying out a qualitative analysis of the histograms.

Having spread the three Luv space channels of the image apart, their histograms are extracted. Each of them is smoothed to suppress unwanted asperities by convolving a Gaussian smoothing kernel with the signal. This is achieved by building a Gaussian window whose parameters are standard deviation (σ) and length. After experimental tuning and the way parameters are related, they are set to $\sigma = 1$ and a length of 6σ. The final filter is a normalization of this one, obtained by dividing it by a sum of all its components.

$$F(x, \sigma) = f(x) * g(x, \sigma) \tag{3.5}$$

Having smoothed each histogram, first and second derivatives are obtained in order to find peaks and valleys. The histogram peaks represent the number of preclusters and are localized as in (3.6). Valleys, thresholds candidates, satisfy (3.7).

$$F_x(x, \sigma) = f(x) * \frac{\partial g(x, \sigma)}{\partial x} = 0, \qquad F_{xx} < 0 \tag{3.6}$$

$$F_x(x, \sigma) = f(x) * \frac{\partial g(x, \sigma)}{\partial x} = 0, \qquad F_{xx} > 0 \tag{3.7}$$

After finding peaks and valleys for each chanel, preclusters must be built. These are called preclusters because definitive clusters refer to regions through all three Luv chanels; segments as a whole. The main requirement is the definition of thresholds

Table 3.2: Coarse segmentation results for the image shown in Fig. 3.12b

Initial nonzero classes	Number of pixels	Class mean Luv values L	u	v	Assigned Color
1	44	0.3240	0.3564	0.0241	Red
9	188,659	0.3277	0.3585	0.1473	Orange
25	787	0.2875	0.3587	0.4602	Yellow

Number of image pixels: 200,253; unclassified pixels: 10,763.

that determine whether a pixel is inside a region or in the fuzzy membership zone. Each of these preclusters is separated from its neighbors by a secure-zone.

$$\begin{aligned} t_{\text{low}} &= \text{peak}(i) \cdot \text{sec-zone} + (1 - \text{sec-zone}) \cdot \text{valley}(i-1) \\ t_{\text{high}} &= \text{peak}(i) \cdot \text{sec-zone} + (1 - \text{sec-zone}) \cdot \text{valley}(i) \\ i &= 1, \ldots, n \end{aligned} \tag{3.8}$$

Here, t_{low} and t_{high} are the precluster's lower and higher thresholds, peak and valley refer to the peak and valley locations in the histogram, and n is the number of preclusters (classes) that exist in each of the three histograms. The histogram regions, which are bounded by a pair of unrelated thresholds, are considered as ambiguous regions. These regions will be further processed in the fine segmentation stage. By changing the secure-zone value (assumed to be between 0 and 1), which is a configurable parameter of the segmentation algorithm, the peaks' overlapping extent can be readily adjusted, and thus the number of the image pixels, which are allocated to the ambiguous regions. Furthermore, secure-zone parameter used in (3.8) was set to 0.4 by recommendation of the author of the method.

The final step of coarse segmentation is to build definitive clusters. The three-coordinate Luv space can be partitioned into several hexahedra obtained as cartesian products of peak intervals found for each color component. These are conformed by going through each precluster and checking its pixels belonging to preclusters of other color components (L, u and v). The maximum number of possible 3-D peaks (clusters) is calculated as the product of the three numbers of peaks in each component. The number of valid clusters, their coordinates in the two-dimension image space and their corresponding mean vectors that are then utilized in the fine stage can be obtained.

After intersecting memberships for each pixel, some of them are not clustered: those outside secure-zones in the first place and those outside hexahedra defined as clusters. These pixels, which are not assigned to any valid clusters, are entered into ambiguous regions, and their fine segmentation is achieved within FCM clustering [95].

3.4.2.2 Fine segmentation

In the fine stage, FCM assigns any remaining unclassified pixels (pixels from ambiguous regions) to the closest cluster based on a weighted similarity measure between the pixels in the image and each of C (e.g., exudates and nonexudates) cluster based on FCM clustering centers [96]. Local extrema of this objective function are indicative

of an optimal clustering of the image. The function is defined as

$$J_{FCM}(U, v; X) = \sum_{k=1}^{n} \sum_{i=1}^{C} (\mu_{ik})^m \|x_k - v_i\|^2, \qquad 1 \leq m < \infty \tag{3.9}$$

where μ_{ik} is the fuzzy membership value of a pixel k to class i and $X = x_1, \ldots, x_n$ is a finite dataset in $\mathbb{R}^d$. $\{v = v_1, \ldots, v_c\}$ is a set of class centers, where $v_i \in \mathbb{R}^d, 1 \leq i \leq C$, represents a d-dimensional ith class center, and is regarded as a prototype. The objective function (3.9) is minimized when high membership values are assigned to pixels whose values are close to the centroid for its particular class, and low membership values are assigned when the pixel data are far from the centroid. Taking the first derivatives of (3.9) with respect to μ_{ik} and v_i, and setting them to zero yields necessary conditions for minimizing the objective function. The parameter m is a weighting exponent that satisfies $m > 1$ and controls the degree of fuzziness in the resulting membership functions. As m increases, the membership functions become increasingly fuzzy.

According to the referenced paper, the value of m was assumed to be equal to 2, and the norm operator represented the standard Euclidean distance. For $m > 1$, local minimum can be defined using the following equations:

$$\begin{aligned} \mu_{ik} &= \frac{1}{\sum_{j=1}^{C} (\|x_k - v_i\| / \|x_k - v_j\|)^{2/(m-1)}} \qquad \forall i, k, \\ v_i &= \frac{\sum_{k=1}^{n} (\mu_{ik})^m x_k}{\sum_{k=1}^{n} (\mu_{ik})^m} \end{aligned} \tag{3.10}$$

where the positive-definite matrix U is the fuzzy C partition of the input image pixels over the set of C cluster centers treated as vectors and v_i represents the ith class center. An important parameter in an FCM clustering algorithm is the number of classes (C) and their corresponding centers that are computed within the coarse segmentation stage. Hence, in this approach, there is no need to recompute the class centers v_i for exudate and nonexudate classes by using (3.10), and instead they are considered as sufficiently well approximated within the coarse segmentation phase.

Table 3.3: Fine segmentation results for the image shown in Fig. 3.12c

Final	Number of	Class mean Luv values			Assigned
nonzero classes	pixels	L	u	v	Color
1	$44 + 4,449 = 4,493$	0.3364	0.3485	0.0512	Red
9	$188,659 + 4,202 = 192,861$	0.3210	0.3528	0.1397	Orange
25	$787 + 2,112 = 2,899$	0.2914	0.3584	0.3822	Yellow

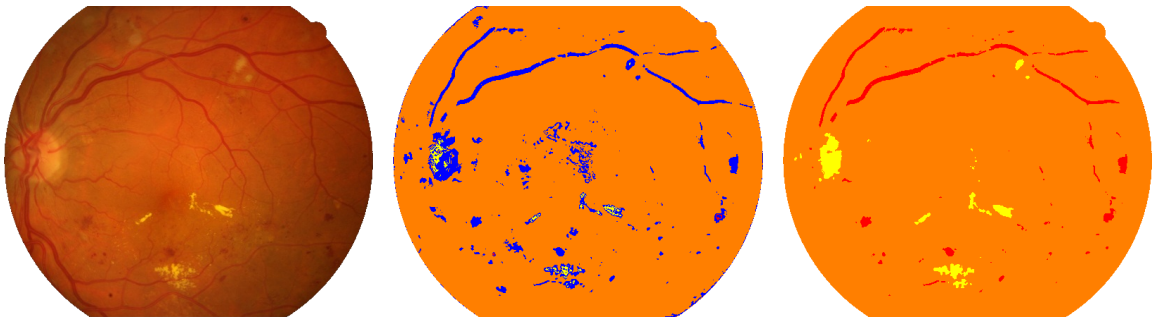

(a) (b) (c)

Figure 3.12: Color segmentation results. (a) Original image. (b) Coarse segmentation result. (c) Fine segmentation result.

At this stage, pixels from ambiguous regions are assigned to the remaining clusters. Thus, for any unclassified pixel x with the feature vector x_k, the fuzzy membership function μ_{ik} is computed, which evaluates the degree of membership of the given pixel to the given fuzzy class $v_i, i = 1, \ldots, C$. The resulting fuzzy segmentation is converted to a hard segmentation by assigning each pixel solely to the class that has the highest membership value for that pixel. As most pixels are classified in the coarse stage, a significant computation time required for FCM is saved.

Fig. 3.12b shows the coarse segmentation result for our running example retinal image. There are three final groups of clusters, i.e., background (orange), blood vessels/red lesions (red), and bright lesions (yellow), in addition to the unclassified pixels, which are marked in blue. The final segmentation result is shown in Fig. 3.12c. It is apparent that the actual bright lesions and some FPs, including OD regions, are included in the candidate bright lesions group of clusters. FP bright lesion regions arise because of other pale objects including retinal light reflections, and most significantly, the OD. The light reflection artifacts, mostly along large blood vessels, are an important source of FPs. Thus, it is crucial to distinguish true bright lesions using a region-based classification scheme, but prior to that the FP OD regions are removed from the other segmented regions using the described automatic OD localization technique (Section 3.3).

3.4.3 Feature extraction and selection

Once the color retinal images are segmented, each image is represented by its corresponding segmented regions. These regions, however, need to be identified in terms of exudates and nonexudates. This is attempted, in a bottom-up approach, by extract-

ing a set of features for each region and classifying the regions based on the generated feature vectors.

Before extracting the feature vector from any region, the pixels corresponding to the OD area must be identified and masked. OD regions are some of the most common false positive exudate regions and are sometimes included in the candidate exudates clusters, because of its pale appearance. Thus, it must be masked in this stage, removed from the other segmented regions using a proposed automatic OD localization technique explained in Section 3.3. This is done after segmentation because bright regions help emphasize lesions clusters in the coarse stage, and before feature extraction because otherwise it would obstruct artificial learning training when it comes to feature characterization (e.g., shape, size).

To select a suitable set of features, it is necessary to take advantage of any prior knowledge of exudates and identify the characteristics that make them distinctive. Clinically, ophthalmologists use color to differentiate between various pathological conditions. Here, region color is also consider as one of the main features. Further features, such as size, edge strength, and texture are also considered.

Table 3.4 shows the final features vector. Initially, a 124 features vector was considered by the author. Nevertheless, 59 of them where discarded according to a genetic algorithm (GA) based selection. This is consistent with the fact that the classification process shall be based on a small number of significant features that effectively characterize the input data and an exhaustive search over all possible combinations of input features is quite expensive. Results of this approach were used to select features 1 through 12 (originally 1–16), the subset that gave the best classification results, but the rest of them were selected differently. After studying GA applications [97, 98] and principal component analysis, it was decided, due to computation time and redundancy, another path was to be taken. This is explained extensively further in the subsection.

Table 3.4: Set of features considered to discriminate bright lesions regions from other segmented regions

Feature	Description
1	Compactness of the region
2	Region size
3	Region edge strength
4–6	Mean Luv values inside the region
7–9	Mean Luv values outside the region
10–12	Standard deviation of Luv values inside the region
13–66	Region mean Gabor filter responses

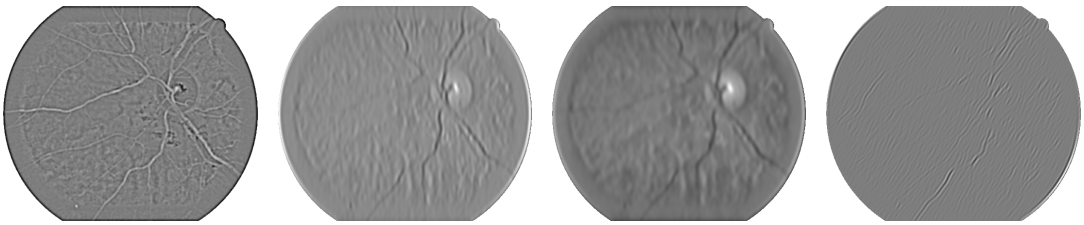

(a) **(b)** **(c)** **(d)**

Figure 3.13: Edge detection and Gabor filters application. All images correspond to further processing of the example in Fig. 3.11a; first one for edge strength detection and the other three for Gabor filters responses. (a) After applying LoG operator. (b) $\theta = 0°$, $\lambda = 2.5$, $\sigma = 5$; (c) $\theta = 0°$, $\lambda = 3.5$, $\sigma = 5$; (d) $\theta = 15°$, $\lambda = 1.5$, $\sigma = 5$.

The first set of features can be described intuitively. Compactness is the ratio of the square of the perimeter to the area of the region. This is, for each region, pixels around each 2-D subregion (regions can be disjoint within themselves on the spatial plane) are added, forming the perimeter. Region area or size is the number of pixels in the cluster. A gray scale version of the image is used.

For region edge strength features, studies were made among different techniques [99, 100], the Laplacian of Gaussian (LoG) operator was chosen [49]. Fig. 3.13a shows LoG filter response of the whole image, where edge pixels result as a high values (bright), while the rest of them derive in low magnitudes (dark). Thus, mean values through each region are computed and stored as the feature of interest. A gray scale version of the image is used in this case also.

While mean and standar deviation values inside and outside the region are explained by themselves, Gabor filter responses require some further analysis. Gray scale image is taken into account again convolved with the following isotropic 2-D Gabor function [52]:

$$g_{\theta,\lambda,\sigma}(x,y) = \exp\left\{-\frac{x^2+y^2}{2\sigma^2}\right\}\exp\left\{\frac{j\pi}{\lambda}(x\cos\theta + y\sin\theta)\right\}. \tag{3.11}$$

The parameter θ represents filter orientation, λ is the filter's wavelength that modifies the sensitivity to high/low frequencies, and σ characterizes the filter standard derivation and equivalently represents scale value. With this parameterization, the Gabor function does not scale uniformly when σ changes. Thus, it is preferable to use a new parameter $\gamma = \lambda\sigma^{-1}$ instead of λ, so that a change in σ corresponds to a true scale change in the Gabor function.

Here, to encode appearance of FCM-based segmented regions in terms of texture,

and thus discriminate more accurately the exudate regions from other nonexudates, a Gabor filter bank is used. In the original approach, this bank contained 108 filters: 12 orientations (θ spanning from 0° up to 180° at steps of 15°), three wavelengths ($\gamma = 1.5, 2.5, 3.5$), and three scales ($\sigma = 3, 5, 7$). The wavelength and scale values are experimentally tuned according to prior knowledge of retinal image characteristics. The response of such a filter bank to an input image is a set of filtered images. In order to select the most representative set of filters, θ was finally spanned from 0° up to 180° at steps of 30° instead of 15°, appealing to redundant responses. This resulted in 54 filters (and therefore, responses and features). Some of them are graphically available in Fig.3.13b–3.13d.

As was discussed in a previous section, the FCM-based segmentation approach segment each input image, yielding a set of image regions. The use of regions enables higher level concepts such as compactness, size, among others, to be considered. In addition to these features, the responses of all Gabor filters (filtered images) is taken into consideration for each segmented region. To do that, the mean responses across the region for each filter is taken. This assigns a 54-element feature vector to each segmented region; a 66-element feature vector overall, as in Table 3.4.

3.4.4 Region level classification

To classify the segmented regions, a well-known NNs discriminative classifiers is exploited [61]. Having selected the optimum feature set based, a corresponding 66-D feature vector (comprising features from Table 3.4) is computed for each segmented region. The multilayer perceptrons NN with three layers has a 66-node input layer corresponding to the feature vector. The optimum proposed architecture has 12 hidden units, with the best performance in terms of the overall generalization ability. All networks are trained using backpropagation learning method. A single output node gives the final classification probability, and the sigmoid activation functions are used in the hidden and output layers.

3.5 Red Lesions Detection

Microaneurysms are the first clinical sign of diabetic retinopathy. The number of microaneurysms is used to indicate the severity of the disease. Early microaneurysm and red lesions detection can help reduce the incidence of blindness. An approach that investigates a set of optimally adjusted morphological operators used for red lesions detection on non-dilated pupil and low-contrast retinal images is selected and

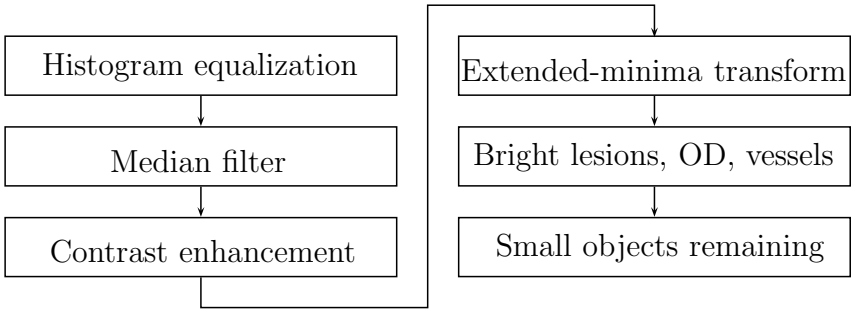

Figure 3.14: Red lesions detection method. Before final detection step, objects detected in previous three sections of this chapter are extracted from the analyzed field of the image.

implemented [80], making some changes in order to adapt it to an image-based approach.

Red lesions detection can be used to grade the DR stage into four stages: no DR, mild DR, moderate DR, and severe DR [13] as shown in Table 3.5.

The system has three main steps. The preprocessing step includes histogram normalization, noise removal and contrast enhancement. Candidate retinal features which may cause a false detection, i.e., exudates and vessels (plus OD) are extracted in the second step. And the last step is red lesions detection by using a set of optimally adjusted mathematical morphology. The overall procedure of red lesions detection is shown in Fig.3.14.

In this section 155 images were used; 89 of them were labeled as normal and 66 of them presented some stage of red lesion manifestation. No training phase is needed.

3.5.1 Preprocessing

Retinal images used in this experiment have poor contrast, noise and non-uniform illumination. A preprocessing step is needed to improve the image quality prior to the detection step. The green plane of the original image in RGB plane is used as red lesions and blood vessels have the highest contrast with the background in this color plane [101].

This is shown in Fig. 3.15, which represents image in original RGB image, red plane, green plane and blue plane, respectively. The first step once selected the green plane is an histogram equalization, normalizing all images to a typical color sample image. A median filtering operation [92] is applied on the green plane to attenuate the noise

before a Contrast Limited Adaptive Histogram Equalization [102] was applied for contrast enhancement.

3.5.2 Bright lesions, vessels and optic disc extraction

This step, although described before morphological operators, is implemented just before they are applied. Nevertheless, it is considered as a previous stage from actual red lesions detection.

Red lesions detection is the main purpose, however bright lesions such as exudates need to be removed prior to the process because when they lie close together, small islands are formed between them and they can be wrongly detected as red lesions. Methods explained in Section 3.4 discriminate pixels corresponding to this issue. Thus, they are removed from analyzed area.

Vessels are another element in the image that needs to be removed prior the red lesions detection since red lesions and vessels both appear in a reddish color and red lesions cannot occur on vessels. They appear as isolated patterns and disconnected from the vessels. To detect vessels, methods described in Section 3.2 result in a binary vessel map. Pixels marked as vessels are then extracted as well.

Taking into consideration vessel segmentation inaccuracy (inclusion of nearly any reddish mark) and disjointed vasculature (because of brighter sections), vessel pixels removal needs to be refined. Using binary vessel map as the input, actual vessels are separated from the rest of the detected pixels. First, vasculature is assumed to be a large connected object, so the biggest region is discarded as false detection. After this, every other isolated region is examined by a major axis length property (*axis* in (3.12)); a scalar specifying the length (in pixels) of the major axis of the ellipse that has the same normalized second central moments as the region. When a region satisfies the condition in (3.12), it is as well discarded as correct vessel detection and

Table 3.5: Criteria used for grading diabetic retinopathy according to red lesions

DR stage	Condition
Grade 0 (no DR)	MA = 0 and H = 0
Grade 1 (mild)	$1 \leq$ MA ≤ 5 and H = 0
Grade 2 (moderate)	$5 <$ MA < 15 or $0 <$ H ≤ 5
Grade 3 (severe)	MA ≥ 15 or H > 5

MA = microaneurysm, H = haemorrhage

(a) (b) (c) (d)

Figure 3.15: RGB bands contrast with the background in retinal images. (a) Original image. (b) Red plane. (c) Green plane. (d) Blue plane.

therefore not removed.

$$(area < 10) \vee \left(\frac{min\{area, axis\}}{max\{area, axis\}} < 0.5 \right) \tag{3.12}$$

As a result, there are some small isolated objects left. Because of error associated with blood vessel detection, bright branching of the vasculature near or above OD region remains after first two steps of extraction. Therefore, OD pixels detected in Section 3.3 are also removed before red lesions detection.

Finally, small segments belonging to any of the above mentioned objects may remain uncleared from the background and therefore may still cause false red lesions detection. Therefore, preliminary isolated regions resulting from morphological operators usage are examined for their area (region size). After objects removal steps, regions whose size decreased are removed entirely. This, understanding they are not overlapped with red lesions pixels. Results are shown in Fig. 3.16d.

3.5.3 Lesion classification

Retinal microaneurysms are focal dilatations of retinal capillaries. They are discrete, localized saccular distensions of the weakened capillary walls and appear as small round dark red dots on the retinal surface. According to the medical definition of microaneurysms [13,103], it is a reddish, circular pattern with a diameter $\lambda < 125\mu m$. The aim is to find a red lesion by its diameter and isolated connected red pixels with a constant intensity value, and whose external boundary pixels all have a higher value; in the green plane of a RGB image.

A preprocessed retinal image is used as preliminary image for red lesions detection. The extended-minima transform is the regional minima of h-minima transform [104]. It is applied to the image. This transformation is a thresholding technique that brings

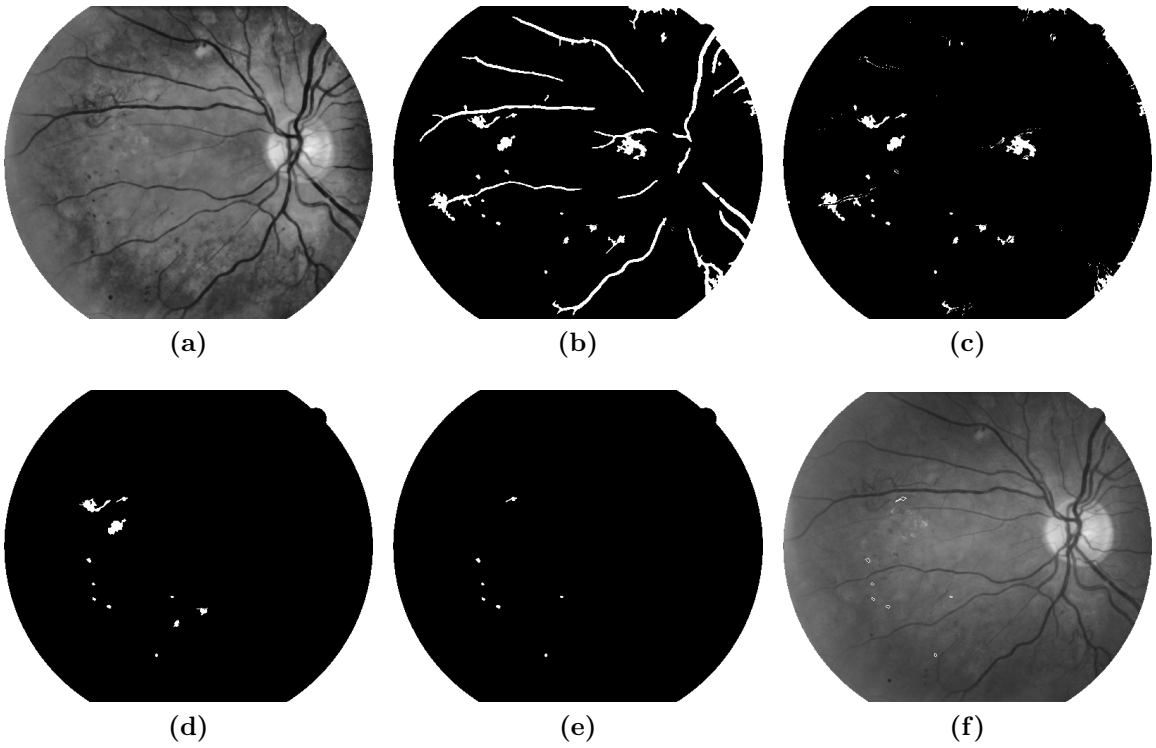

Figure 3.16: Red lesions detection intermediate results. (a) Image after histogram equalization, median filter and contrast enhancement application. (b) Extended-minima transform. (c) Bright lesions, OD and vessels removal. (d) Remaining segments cleansing. (e) Detected red lesions sized bellow 50 pixels. (f) Lesions delineated (white) over original image G band.

most of the valleys to zero. The h-minima transform suppresses all the minima in the intensity image whose depth is less than or equal to a predefined threshold. The output image is a binary image with the white pixels represent the regional minima in the original image. Regional minima are connected pixels with the same intensity value, whose external boundary pixels all have a higher value. The output is a binary image. The extended minima transform on the image has a threshold value α.

The selection of threshold is very important where the higher value of α will lower the number of regions and a lower value of α will raise the number of regions. The result is shown in Fig. 3.16b. A slight change in threshold value can cause the method either over-segment or under-segment the red lesions. The previous detected bright lesions, OD and vessels were removed from the resulting image. The result is shown in Fig. 3.16c.

Then the objects with a size smaller or equal to 50 pixels are selected and classified

as red lesions. The result is shown in Fig. 3.16e.

There are parameters used in this experiment. They are, namely, the size of structuring element (B) used for the closing operation, threshold value (α). B and α were varied and tested in order to assess the algorithm performance in an experiment. All parameters in this proposed method are set using the values that gave highest sensitivity and specificity in the previous experiment. The experiment showed that the value of $B = 50$ and $\alpha = 28$ gave a good balance between the number of detected red lesions and the number of detected spurious objects.

Chapter 4

Results and Discussion

All methods were applied in our database and therefore are not comparable to universal published databases. For this purpose, 285 images had been labeled in terms of OD (and fovea) center location and pixels corresponding to bright lesions. They have been divided in 143 training images and 142 testing images. 155 images were classified in terms of presence of red lesions.

Blood vessels segmentation results could not be analyzed because images were not labeled at a pixel-level. Therefore, performance is later shown as intermediate result in the other sections of the process. This is the case of the novel intermediate processing for red lesions detection, in order to reduce wrongly detected vessels. This step takes 14.19 seconds in average per image.

For OD localization, the evaluation criteria used in the literature has been used. Counting OD detections inside the diameter of the OD as a true detection is an accepted evaluation method used by several of the references [68, 105, 106]. For this application, DR screening, knowing only the approximate center point of both structures is adequate as there is no interest in the exact OD segmentation but simply mask it.

OD localization results are shown in Fig. 4.1, marking ground truth object with a circumference (centered in OD center marked by specialist, radius 50 pixels) and the automatically estimated center with a black square.

Cases in which the OD location is less precise have been examined. The majority of failed detections are caused by poor contrast, poor quality vessel segmentation, imaging artifacts and the presence of pathology or a combination of these factors. When the contrast over the OD is low, this not only affects the intensity features but also the vessel segmentation result. This combination of factors may prevent the

system from extracting appropriate features for OD localization.

For each image it was determined whether the OD location found by the algorithm was inside the border of the OD as indicated in the ground truth. The 142 testing samples were conformed by 107 normal images and 35 abnormal images. Accuracy was 100%, because each of the estimations were inside the diameter of 50 pixels. Average error distance was 10.70 pixels, with a standard deviation of 5.91, minimum of 0 and maximum of 30.08 pixels. The average runtime was 2.02 minutes.

To investigate the effectiveness of the bright lesions detection method, the same image dataset of 285 labeled retinal images including 214 normal and 71 abnormal images is considered. To evaluate the efficiency of the proposed region-level classification scheme including image preprocessing, FCM-based segmentation, and NN-based classification, 36 abnormal and 107 normal images from the image dataset are considered. The remaining 142 images are utilized as unseen images to validate the effectiveness of the bright lesions recognition approach in terms of both image-based and pixel-resolution accuracies. The segmentation scheme begins by Gaussian filtering of Luv histograms of this image to derive the number of clusters and approximate the location of their centers. The segmentation algorithm requires two parameters, i.e., scale (σ) and secure-zone that need to be defined.

Scale parameter (σ) controls the smoothing extent of the histograms' fine structures. By reducing the value of this parameter, the histogram smoothing degree is decreased, thus, the fine structures are less suppressed. The secure-zone parameter has a direct effect in evaluating the lower and higher threshold values, it thus influences the pixels number, which are allocated to the ambiguous regions and passed to the fine segmentation stage.

Here, the optimum σ and secure-zone values are experimentally tuned ($\sigma = 1 \Rightarrow \alpha_{gausswin} = 2.5$, secure-zone $= 0.4$) Indeed, to avoid discarding any true lesions pixels, these parameters are adjusted in favor of more FPs than FNs.

Having set the segmentation parameters, the technique is applied to all 142 images using $\sigma = 5$ and secure-zone $= 0.4$, respectively. This results in 1235 segmented regions. These regions are then labeled by an expert ophthalmologist as 245 bright

Table 4.1: Bright lesions region-level detection results. Perceptron threshold varies between 0 and 0.5.

	Threshold										
	0	0.05	0.1	0.15	0.2	0.25	0.3	0.35	0.4	0.45	0.5
Sensitivity	0.98	0.97	0.95	0.94	0.91	0.86	0.84	0.80	0.74	0.69	0.64
Specificity	0.22	0.45	0.60	0.68	0.76	0.80	0.85	0.88	0.91	0.93	0.95

lesions and 990 nonlesions. The segmented regions are divided into separate training, validation, and test sets. Among several NNs containing varying numbers of hidden units that are trained, a network, with 12 hidden units performs best in terms of the overall generalization ability. Results given by the classifying perceptron is a posterior probability between 0 (nonlesion) and 1 (lesion). Its threshold can be tuned, as shown in Table 4.1.

So far, region-level classification of a set of segmented regions using NN classifiers has been discussed. The trained classifiers can also be used to evaluate the effectiveness of the bright lesions recognition approach in terms of both introduced image-based and pixel-resolution accuracies. Then a final decision is made as to whether the image has some evidence of retinopathy in terms of bright lesions. Again, the threshold can be tuned, as shown in Table 4.2.

Threshold is fixed with experts to obtain more FPs and a decent amount of FNs (0.3). This classifier achieves an overall 84.08% sensitivity and 84.65% specificity in terms of regions classification. The proposed system can identify affected retinal images with 91.43% sensitivity (correct classification of 32 abnormal images out of 35) while it recognizes 53.27% of the normal images, i.e., the specificity (correct classification of 57 normal images out of 107).

Improvable issues in this subject can be divided in two: segmentation and classification. Segmentation problems are responsible for system's region-based misclassification as well as expert mislabeling. Classification errors are plain NN malfunction.

Segmentation issues occur because bright nonlesion regions of the image are clustered together with lesions. In some cases this can be fine-tuned going through parameter definition and processing techniques, but this also happens when a significantly bright region at the edge of the image appears. In this case, the problem is not the system, but the image acquisition, as the patient moves slightly away from the camera and lets additional light beams into the lens.

Classification issues have been found to occur because of the lack of training samples, as the total dataset must be divided into training, validation and testing sets. Once divided, images can be normal and abnormal. Obviously, abnormal images consist of

Table 4.2: Bright lesions image-level detection results. Perceptron threshold varies between 0 and 0.5.

	Threshold										
	0	0.05	0.1	0.15	0.2	0.25	0.3	0.35	0.4	0.45	0.5
Sensitivity	1.00	1.00	1.00	1.00	0.97	0.91	0.91	0.89	0.83	0.83	0.77
Specificity	0.00	0.02	0.09	0.21	0.35	0.42	0.53	0.64	0.70	0.78	0.84

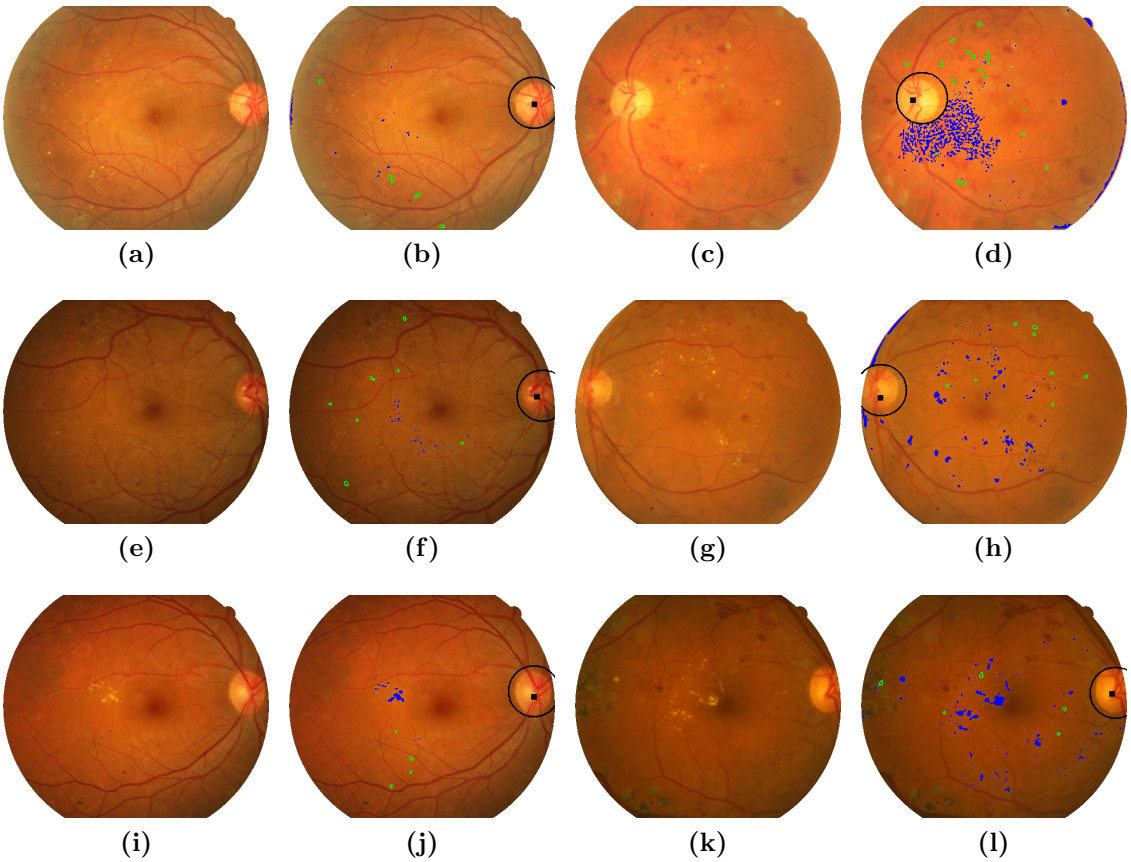

Figure 4.1: Diabetic retinopathy detection results. Odd columns show original images and even columns show: OD localization (square) and actual position (circular object); bright lesions detection (blue); red lesions detection (green).

lesion and nonlesion regions. Therefore, bright lesion images are very few, resulting in a small amount of abnormal regions for quality generalization when training with 245 clusters.

In terms of computational speed, bright lesions identification method takes, on average, 7.34 minutes for processing each image. This is 2.52 minutes in preprocessing and segmentation, and 4.80 minutes in feature extraction and classification. This time performance can be improved through a more efficient implementation, especially when applying convolution with filters, e.g., Gabor.

The fourth and final phase is red lesions detection. This step is somewhat different from those that precede, as it does not need a training dataset. On the other hand, a specific set of images was selected for this purpose: they must belong to the testing

set of the previous stages in order to evaluate the system as a whole, and the presence or absence of red lesions should be very accurate.

As mentioned above, previously detected landmarks is a crucial requisite of this step, as corresponding regions are removed from analysis before morphological operation and classification. 89 normal and 66 abnormal images were processed, performing 96.97% and 92.13% of sensitivity and specificity respectively. This is in an image-based approach, so it means 82 out of 89 normal images were correctly classified and 64 of 66 abnormal images were correctly detected.

Due to red lesions image (and not pixel) approach, lesions may remain undetected without being reflected in the performance indicators. This would be critical in a computer-aided diagnosis, but for screening purposes it is not. In any case, This can be improved as well as specified in terms of the size/severity of the lesion: for first time examined patients, asymptomatic lesions presence should not manifest as significantly large haemorrhages.

Red lesions detection took 0.22 seconds to process each image. This includes every other region removal and specific procedures, but not vessels, OD and bright lesions specific ones.

System overall results are estimated in 88.66% specificity and 49.08% sensitivity for DR detection at an image level. Examples on abnormal images are shown in Fig. 4.1.

The whole procedure takes, on average, 10 minutes for processing each image using straightforward MATLAB implementation for tests. Retinal images are tested on an Intel Core i5 2.53 GHz with 6 GB memory.

Chapter 5

Conclusions and Future Work

This work concentrates on bright lesions and red lesions detection from DR patients' non-dilated pupil digital retinal images as a preliminary phase of an automated DR screening system. The system intends to help the ophthalmologists in the DR screening process to detect symptoms faster and more easily. Each of the main stages of the system summary is presented, followed by specific stages recommendations and general suggestions for future work.

The tool is oriented to make the health system more efficient and effective, allowing massive retina screening for diabetic patients and demanding ophthalmologists intervention only in certain cases. These cases are reduced to the ones that involve algorithm detection of structures that may note disease manifestation.

For blood vessels localization, the Gabor transform shows itself efficient in enhancing vessel contrast, while filtering out noise. Information from Gabor transforms at different scales, which allows the segmentation of vessels of different diameters, are integrated through the use of the statistical classifier presented. The GMM classifier has a computationally demanding training phase, but guarantees a fast classification phase and good performance. Furthermore, the methods are conceptually simple and can be implemented efficiently.

A drawback of this approach is that it only takes into account information local to each pixel through image filters, ignoring useful information from shapes and structures present in the image. This drawback is addressed by methods applied in red lesions detection intermediate results. Thus, automated segmentation of fundus images provides the basis for automated assessment by community health workers.

An automatic step for OD location detection has been developed. The system uses a kNN regressor and a circular template to estimate the distance to a location in

the image. The performance of the system is satisfactory, in a heterogeneous set of regular screening images it successfully detected the location of the OD in all cases.

For a screening application, the main effect of a misdetected OD is that it will not be masked out correctly. This will in turn lead the abnormality detection algorithms to detect abnormalities on the OD location. This can cause a normal image to be flagged as potentially abnormal, which would lead to more work for the screening ophthalmologist.

The current performance of the OD detection system leads to believe it is ready to be applied in an automated DR screening system. As long as the preprocessing step is done so that the FOV is resized to a standard size, the images are digital color fundus photographs and the coverage of the FOV is either 35° or 45°, the system should not have to be retrained; moreover, the parameter settings as described can be applied.

As a summary, a robust, fast method to detect the position of the OD in retinal images was implemented. The method showed results comparable to state of the art methods and does not make strong assumptions about the location of the anatomical landmark in the image. This makes this step useful in an automated screening system for DR.

Methods toward the development of an automated computational-intelligent-based decision support system for the purpose of detecting and classifying bright lesions pathologies of DR has been explored. In medical decision support systems such as this approach, an accurate diagnostic accuracy assessment in terms of both pixel-resolution and image-based is essential.

Here, bright lesions are located at pixel level in color retinal images. The diagnostic accuracy of the method is evaluated in terms of both pixel-resolution and image-based criteria. Robustness and accuracy in comparison to expert ophthalmologists have been evaluated on a relatively large image dataset. Indeed, advantage is taken of retinal pathology–anatomical parts color information toward the objectives, and show the improvement obtained over gray-level-based techniques. The high performance of the proposed method is in part enabled by the integration of several efficient computational-intelligence-based methods, especially FCM color segmentation, and NN classifiers. Another important aspect of this study is that it tackles the varying retinal color, which may be due to skin pigmentation and iris color. In fact, without some type of color normalization, the larger variation in the natural retinal pigmentation across the patient dataset can hinder discrimination of the relatively small variations between the different lesion types. Thus, a color normalization method is applied to make the images invariant with respect to the background pigmentation variation and the bright lesion color variation between individuals.

Bright lesions step indicates that automated diagnosis of bright lesions retinopathy

using combination of computational intelligence techniques and color retinal image analysis is very successful in detecting bright lesions. Hence, the system can be used to evaluate digital retinal images obtained in screening programmes for DR and operated by nonexperts (only for image acquisition), reaching an outcome about which patients require referral to an ophthalmologist for further investigation and treatment. The bright lesions large majority can be detected, and also most of the normal images can be correctly identified by the selected method. This provides a huge savings in terms of the number of retinal images that require to be manually reviewed by the medical professionals.

Red lesions detection step could perform on very poor quality images. There are some incorrect lesions detections which are caused by the artifacts, too small lesions, too blurred lesions, faint blood vessels which cannot detected/removed or lesions that appear very faint. There are some missing lesions located next to or nearby blood vessels which are removed as wrongly detected as blood vessels. They are also faint blood vessels which are not removed in vessel detection step; lesions could be wrongly detected on those vessels. The results of lesions detection depend on the success of vessel detection. A main weakness of the algorithm arises from this fact. This indicates the further necessity of improving the robustness of this task. Although future development of this algorithm is still required, the results are satisfy our expectations.

Regarding future work continuity, some recommendations after results analysis can be exposed. In case of blood vessels segmentation, a larger training database should be used. A reduced one was used for this work purposed due to time restrictions, but an increased one could train a classifier that would surely improve generalization and pixel segmentation results.

Bright lesions detection had the least satisfactory performance indicators. This also allows a considerable amount of improvements. In the preprocessing step, histogram normalization may be evaluated experimentally by varying its reference image (histogram). This could lead to a more suitable color reference and therefore segmentation. Another necessary step to perform before contrast enhancement is a mirror operation processing for removing undesired border effects. That way, FOV edge would not interfere with contrast enhancement and thereby with segmentation.

Another phase of bright lesions detection that needs to be upgraded is the segmentation and feature extraction. Optimization of the coarse segmentation can be accomplished by removing pixels outside the FOV (black). Also, histogram smoothing parameter σ variation can be explored. Differences in the classification results may be studied when removing OD pixels before segmentation instead of after. Regarding computing time and efficiency, improved code could impact positively, especially for filters convolution with the image when extracting regions' features.

A critical aspect in bright lesions detection approach is the training dataset. This work uses a small number of images, so it is crucial to increase labeled samples for the training phase to work better. Test-training images swap proved that classification results improve significantly when this increase is carried out.

A more sophisticated approach could be accomplished establishing the spatial relationship between the detected bright lesions and central macular area (fovea). This is because bright lesions and edema occurring more than 500μm from the fovea, do not necessarily need treatment with the laser because they are not immediately sight-threatening, and may disappear spontaneously. To do this, fovea location methods can be added using the same approach selected for OD localization [70].

Larger red lesions (mainly haemorrages) not detected could be included if fovea is located and removed, implementing the approach mentioned above. Small lesions not detected are mostly discarded as blood vessels, so improvement in this matter should lead to improvement in lesions detection at pixel-level.

Overall recommendations are also useful. First of all, improvements in code implementation may always reduce computing time and efficiency. Once this step is developed, implementing the system in an embeddable programming language may save up time if the objective is further application at customer's end.

An additional main stage, prior to the first of the four developed in this work (blood vessels localization, OD localization, bright and red lesions detection), is a quality test that allows to automatically discard images with insufficient image quality [13, 14]. That way, system would train and test itself only in samples that have enough features to be processed as they are supposed to, avoiding errors due to image acquisition flaws. These include light excess or lack, blurred samples, among other reasons why system fails in its outcomes, not its processing.

Technology, at its current stage or with described further improvements, should be packaged. Every step should be connected with each other into the process as a whole, developing upgrades and possible specific improvements.

In the same way, a functional prototype may be implemented for specialist to correct. This interaction will help spot which exact stage of the developed process caused it's failure at certain degree. If well designed, it may also help increasing training database in all of its steps. This implementation is crucial as a clinical validation of the development.

Finally, it is important to interpret performance indicators as business indicators. In other words, link performance of this work with budget, health coverage and specialists savings. This is in order to measure real impact on health system, customers and health field stakeholders in general.

Bibliography

[1] R. N. Frank, "Diabetic retinopathy," *The New England Journal of Medicine*, 2004.

[2] D. M. Broadbent, J. A. Scott, J. P. Vora, and S. P. Harding, "Prevalence of diabetic eye disease in an inner city population: The Liverpool Diabetic Eye Study," *Eye*, 1999.

[3] A. K. Sjolie, J. Stephenson, S. Aldington, E. Kohner, H. Janka, L. Stevens, *et al.*, "Retinopathy and vision loss in insulin-dependent diabetes in Europe. The Eurodiab IDDM Complications Study," *Ophthalmology*, 1997.

[4] T. Y. Wong, R. Klein, F. M. Islam, M. F. Cotch, A. R. Folsom, B. E. Klein, *et al.*, "Diabetic retinopathy in a multi-ethnic cohort in the United States," *American Journal of Ophthalmology*, 2006.

[5] D. Klonoff and D. Schwartz, "An economic analysis of interventions for diabetes," *Diabetes Care*, vol. 23, 2000.

[6] D. S. Fong, L. Aiello, T. W. Gardner, G. L. King, G. Blankenship, J. D. Cavallerano, F. L. Ferris, and R. Klein, "Diabetic retinopathy," *Diabetes Care*, vol. 26, 2003.

[7] J. K. Kristinsson, "Diabetic retinopathy, screening and prevention of blindness. A doctoral thesis," *Acta Ophthalmologica Scandinavica Supplement*, 1997.

[8] The Diabetic Retinopathy Study Research Group, "Photocoagulation treatment of proliferative diabetic retinopathy. Clinical application of Diabetic Retinopathy Study (DRS) findings, DRS report number 8," *Ophthalmology*, 1981.

[9] A. Fagot-Campagna, I. Romon, N. Poutignat, and J. Bloch, "Non-insulin treated diabetes: Relationship between disease management and quality of care," *The Entred study*, 2001.

[10] CNAMTS (Caisse nationale d'Assurance maladie des travailleurs salariés), "In rapport sur la démographie en ophtalmologie, de 2000–2020." `http://www.ameli.fr`, 2004.

[11] Centers for Disease Control and Prevention: Data & Trends, "National Diabetes Surveillance System: Preventive care practices, 1994–2004." `http://www.cdc.gov/diabetes/statistics/preventive/tX.htm`, accesed july 8, 2007.

[12] M. D. Abràmoff, M. Niemeijer, M. S. Suttorp-Schulten, M. A. Viergever, S. R. Russell, and B. van Ginneken, "Evaluation of a System for Automatic Detection of Diabetic Retinopathy From Color Fundus Photographs in a Large Population of Patients With Diabetes," *Diabetes Care*, 2008.

[13] B. Dupas, T. Walter, A. Erginay, R. Ordonez, N. Deb-Joardar, P. Gain, J.-C. Klein, and P. Massin, "Evaluation of automated fundus photograph analysis algorithms for detecting microaneurysms, haemorrhages and exudates, and of a computer-assisted diagnostic system for grading diabetic retinopathy," *Diabetes & Metabolism*, 2010.

[14] M. Niemeijer, M. D. Abràmoff, and B. van Ginneken, "Image structure clustering for image quality verification of color retina images in diabetic retinopathy screening," *Medical image analysis*, 2006.

[15] D. S. Fong, L. P. Aiello, F. L. Ferris, and R. Klein, "Diabetic retinopathy," *Diabetes Care*, vol. 27, 2004.

[16] D. S. Fong, L. Aiello, T. W. Gardner, G. L. King, G. Blankenship, J. D. Cavallerano, F. L. Ferris, and R. Klein, "Diabetic retinopathy," *Diabetes Care*, vol. 27 (Suppl. 1), 2004.

[17] D. S. Chia and E. Y. Yap, "Comparison of the effectiveness of detecting diabetic eye disease: diabetic retinal photography versus ophthalmic consultation," *Singapore Medical Journal*, 2004.

[18] Early Treatment Diabetic Retinopathy Study Research Group, "Early photocoagulation for diabetic retinopathy: ETDRS report 9," *Ophthalmology*, 1991.

[19] L. M. Aiello, S. E. Bursell, J. Cavallerano, W. K. Gardner, and J. Strong, "Joslin Vision Network Validation Study: pilot image stabilization phase," *Journal of the American Optometric Association*, 1998.

[20] G. H. Bresnick, D. B. Mukamel, J. C. Dickinson, and D. R. Cole, "A screening approach to the surveillance of patients with diabetes for the presence of vision-threatening retinopathy," *Ophthalmology*, 2000.

[21] R. J. Brechner, C. C. C. L. J. Howie, W. H. Herman, J. C. Will, and M. I. Harris, "Ophthalmic examination among adults with diagnosed diabetes mellitus," *Journal of the American Medical Association*, 1993.

[22] C. Wilson, M. Horton, J. Cavallerano, and L. M. Aiello, "Addition of primary care-based retinal imaging technology to an existing eye care professional referral program increased the rate of surveillance and treatment of diabetic retinopathy," *Diabetes Care*, vol. 28, 2005.

[23] "Diabetes care and research in Europe: The SaintVincent declaration," 1990.

[24] "Association de langue française pour l'étude du diabète et des maladies métaboliques (ALFEDIAM)." `http://www.alfediam.org`.

[25] American Academy of Ophthalmolgy Retina Panel, "Preferred practice pattern: Diabetic retinopathy (article online).," *Diabetes Care*, 2008. `http://www.aao.org/ppp`.

[26] D. Y. Lin, M. S. Blumenkranz, R. J. Brothers, and D. M. Grosvenor, "The sensitivity and specificity of single-field nonmydriatic monochromatic digital fundus photography with remote image interpretation for diabetic retinopathy screening: a comparison with ophthalmoscopy and standardized mydriatic color photography," *American Journal of Ophthalmology*, 2002.

[27] G. A. Williams, I. U. Scott, J. A. Haller, A. M. Maguire, D. Marcus, and H. R. McDonald, "Singlefield fundus photography for diabetic retinopathy screening: a report by the American Academy of Ophthalmology," *Ophthalmology*, 2004.

[28] M. G. Lawrence, "The accuracy of digitalvideo retinal imaging to screen for diabetic retinopathy: an analysis of two digital-video retinal imaging systems using standard stereoscopic seven-field photography and dilated clinical examination as reference standards," *Transactions of the American Ophthalmological Society*, 2004.

[29] P. Massin, K. Angioi-Duprez, F. Bacin, B. Cathelineau, G. Cathelineau, G. Chaine, *et al.*, "Detection, monitoring and treatment of diabetic retinopathy. Recommendations of ALFEDIAM. Committee of above-mentioned experts and validated by the board of directors and scientific board of ALFEDIAM," *Diabetes & Metabolism*, 1996.

[30] N. Deb, G. Thuret, B. Estour, P. Massin, and P. Gain, "Screening for diabetic retinopathy in France," *Diabetes & Metabolism*, 2004.

[31] National Institute of Health, "National Diabetes Statistics, 2011." `http://diabetes.niddk.nih.gov/dm/pubs/statistics/DM_Statistics.pdf`, accesed november 7, 2011.

[32] Comisión nacional del XVII censo de población y VI de vivienda 2003, "Síntesis de resultados censo 2002." `http://www.ine.cl/cd2002/sintesiscensal.pdf`, accesed december 27, 2008.

[33] Fonasa Chile, "Auge en línea - ¿qué enfermedades garantiza?." `http://augeenlinea.fonasa.cl/portal/paginas/queEnfermedades.jsp`, accesed november 7, 2011.

[34] X. Aguilera, C. González, A. Guerrero, P. Bedregal, V. Milosavljevic, M. Rivera, J. Vega, J. Salinas, F. Otaíza, F. Espejo, and C. Espinosa, "Objetivos sanitarios para la década 2000–2010," *El vigía*, 2002.

[35] P. Chapman, J. Clinton, R. Kerber, T. Khabaza, T. Reinartz, C. Shearer, and R. Wirth, "CRISP-DM 1.0 Step-by-step data mining guide," 2000.

[36] G. K. Lang, "Diabetic Retinopathy," *Dev Ophthalmol*, vol. 39, 2007.

[37] G. K. Lang, *Ophthalmology, A Pocket Textbook Atlas*. Thieme, 2nd ed., 2006.

[38] S. Aldington, E. Kohner, S. Meuer, R. Klein, A. SjØlie, and , "Methodology for retinal photography and assessment of diabetic retinopathy: the EURODIAB IDDM Complications Study," *Diabetology*, vol. 38, 1995.

[39] H. Murgatroyd, A. Ellingford, A. Cox, M. Binnie, J. Ellis, C. MacEwen, and G. L. G, "Effect of mydriasis and different field strategies on digital image screening of diabetic eye disease," *Br J Ophthalmol*, 2004.

[40] E. Kohner and M. Porta, "Protocols for screening and treatment of diabetic retinopathy in Europe," *Eur J Ophthalmol*, 1991.

[41] M. Baeza, V. Gil, D. Orozco, V. Pedrera, C. Ribera, I. Pérez, and J. Martínez, "Validez de la cámara no midriática en el cribado de la retinopatía diabética y análisis de indicadores de riesgo de la retinopatía," *Arch Soc Esp Oftalmol*, 2004.

[42] J. C. Russ, *The Image Processing Handbook*. CRC Press, 6th ed., 2011.

[43] H. S. Fairman, M. H. Brill, and H. Hemmendinger, "How the CIE 1931 color-matching functions were derived from Wright-Guild data," *Color Research & Application*, vol. 22, no. 1.

[44] J. Schanda, *Colorimetry: understanding the CIE system*. John Wiley & Sons, 1st ed., 2007.

[45] M. W. Schwarz, W. B. Cowan, and J. C. Beatty, "An experimental comparison of RGB, YIQ, LAB, HSV, and opponent color models," *ACM Trans. Graph.*, vol. 6, 1987.

[46] F. J. Harris, "On the use of windows for harmonic analysis with the discrete Fourier transform," *Proceedings of the IEEE*, vol. 66, 1978.

[47] A. Savitzky and M. J. E. Golay, "Smoothing and differentiation of data by simplified least squares procedures," *Anal. Chem.*, 1964.

[48] J. A. Stark and W. J. Fitzgerald, "An alternative algorithm for adaptive histogram equalization," *Comp. Vis. Graph. Image Proc.*, 1996.

[49] R. Gonzalez and R. Woods, *Digital Image Processing.* Prentice Hall, 3rd ed., 2008.

[50] D. Marr, *Vision.* W. H. Freeman, San Francisco, 1982.

[51] D. Marr and E. Hildreth, "Theory of edge detection," *Proc. R. Soc. Lond.*, vol. 207, 1980.

[52] O. Nestares, R. Navarro, J. Portilla, and A. Tabernero, "Efficient spatialdomain implementation of a multiscale image representation based on Gabor functions," *Journal of Electronic Imaging*, 1998.

[53] S. Theodoridis and K. Koutroumbas, *Pattern Recognition.* Academic Press, 3rd ed., 2008.

[54] L. Devroye, L. Györfi, and G. Lugosi, *A Probabilistic Theory of Pattern Recognition.* Springer-Verlag, New York, USA, 1996.

[55] R. O. Duda, P. E. Hart, and D. G. Stork, *Pattern Classification.* John Wiley & Sons, 2nd ed., 2001.

[56] K. Hattori and M. Takahashi, "A new edited k-nearest neighbor rule in the pattern classification problem," *Pattern Recognition*, vol. 33, 2000.

[57] K. Krishna, M. A. L. Thathachar, and K. R. Ramakrishnan, "Voronoi networks and their probability of misclassification," *IEEE Transactions on Neural Networks*, vol. 11(6), 2000.

[58] T. Mitchell, *Machine Learning.* Mc-Graw Hill, 1997.

[59] J. C. Dunn, "A fuzzy relative of the ISODATA process and its use in detecting compact well-separated clusters," *Journal of Cybernetics*, 1973.

[60] J. C. Bezdek, "Pattern recognition with fuzzy objective function algorithms," *Plenum Press, New York*, 1981.

[61] C. Bishop, *Neural Networks for Pattern Recognition.* London, U.K.: Oxford University Press, 1995.

[62] M. Niemeijer, J. Staal, B. van Ginneken, M. Loog, and M. D. Abramoff, "Comparative study of retinal vessel segmentation methods on a new publicly available database," vol. 5370, pp. 648–656, SPIE, 2004.

[63] S. Dua, N. Kandiraju, and H. Thompson, "Design and implementation of a unique blood-vessel detection algorithm towards early diagnosis of diabetic retinopathy," in *Information Technology: Coding and Computing, 2005. ITCC 2005. International Conference on*, vol. 1, pp. 26 – 31 Vol. 1, april 2005.

[64] J. V. B. Soares, J. J. G. Leandro, R. M. Cesar, H. F. Jelinek, and M. J. Cree, "Retinal vessel segmentation using the 2-D Gabor wavelet and supervised classification," *IEEE Transactions on Medical Imaging*, 2006.

[65] S. Kumar and M. Madheswaran, "Extraction of blood vascular network for development of an automated diabetic retinopathy screening system," in *Computer Technology and Development, 2009. ICCTD '09. International Conference on*, vol. 2, pp. 360 –364, nov. 2009.

[66] M. Lalonde, M. Beaulieu, and L. Gagnon, "Fast and robust optic disc detection using pyramidal decomposition and hausdorff-based template matching," *Medical Imaging, IEEE Transactions on*, vol. 20, pp. 1193 –1200, nov. 2001.

[67] M. Foracchia, E. Grisan, and A. Ruggeri, "Detection of optic disc in retinal images by means of a geometrical model of vessel structure," *Medical Imaging, IEEE Transactions on*, vol. 23, pp. 1189 –1195, oct. 2004.

[68] M. Niemeijer, M. Abramoff, and B. van Ginneken, "Segmentation of the optic disc, macula and vascular arch in fundus photographs," *Medical Imaging, IEEE Transactions on*, vol. 26, pp. 116 –127, jan. 2007.

[69] A.-H. Abdel-Razik Youssif, A. Ghalwash, and A. Abdel-Rahman Ghoneim, "Optic disc detection from normalized digital fundus images by means of a vessels' direction matched filter," *Medical Imaging, IEEE Transactions on*, vol. 27, pp. 11 –18, jan. 2008.

[70] M. Niemeijer, M. D. Abràmoff, and B. van Ginneken, "Fast detection of the optic disc and fovea in color fundus photographs," *Medical image analysis*, 2009.

[71] T. Walter, J.-C. Klein, P. Massin, and A. Erginay, "A contribution of image processing to the diagnosis of diabetic retinopathy-detection of exudates in color fundus images of the human retina," *Medical Imaging, IEEE Transactions on*, vol. 21, pp. 1236 –1243, oct. 2002.

[72] M. Niemeijer, B. van Ginneken, S. Russel, M. Suttorp-Schulten, and M. Abramoff, "Automated detection and differentiation of Drusen, exudates, and cotton-wool spots in digital color fundus photographs for early diagnosis of

Diabetic Retinopathy," *Investigative Ophthalmology & Visual Science*, vol. 48, pp. 2260–2267, 2007.

[73] A. Bin Mansoor, Z. Khan, A. Khan, and S. Khan, "Enhancement of exudates for the diagnosis of diabetic retinopathy using fuzzy morphology," in *Multitopic Conference, 2008. INMIC 2008. IEEE International*, pp. 128 –131, dec. 2008.

[74] A. Osareh, B. Shadgar, and R. Markham, "A Computational-Intelligence-Based Approach for Detection of Exudates in Diabetic Retinopathy Images," *IEEE Transactions on Information Technology in Biomedicine*, 2009.

[75] C. I. Sanchez, M. Niemeijer, M. S. A. S. Schulten, M. Abramoff, and B. van Ginneken, "Improving hard exudate detection in retinal images through a combination of local and contextual information," in *Proceedings of the 2010 IEEE international conference on Biomedical imaging: from nano to Macro*, ISBI'10, (Piscataway, NJ, USA), pp. 5–8, IEEE Press, 2010.

[76] M. Cree, J. Olson, K. McHardy, J. Forrester, and P. Sharp, "Automated microaneurysm detection," in *Image Processing, 1996. Proceedings., International Conference on*, vol. 3, pp. 699 –702 vol.3, sep 1996.

[77] J. H. Hipwell, F. Strachan, J. A. Olson, K. C. McHardy, P. F. Sharp, and J. V. Forrester, "Automated detection of microaneurysms in digital red-free photographs: a diabetic retinopathy screening tool.," *Diabetic medicine : a journal of the British Diabetic Association*, vol. 17, pp. 588–594, Aug. 2000.

[78] D. Vallabha, R. Dorairaj, K. Namuduri, and H. Thompson, "Automated detection and classification of vascular abnormalities in diabetic retinopathy," in *Signals, Systems and Computers, 2004. Conference Record of the Thirty-Eighth Asilomar Conference on*, vol. 2, pp. 1625 – 1629 Vol.2, nov. 2004.

[79] M. Niemeijer, B. van Ginneken, J. Staal, M. Suttorp-Schulten, and M. Abramoff, "Automatic detection of red lesions in digital color fundus photographs," *Medical Imaging, IEEE Transactions on*, vol. 24, pp. 584 –592, may 2005.

[80] A. Sopharak, B. Uyyanonvara, and S. Barman, "Automatic microaneurysm detection from non-dilated diabetic retinopathy retinal images using mathematical morphology methods," *IAENG International Journal of Computer Science*, 2011.

[81] J. Staal, M. Abramoff, M. Niemeijer, M. Viergever, and B. van Ginneken, "Ridge-based vessel segmentation in color images of the retina," *Medical Imaging, IEEE Transactions on*, vol. 23, pp. 501 –509, april 2004.

[82] J.-P. Antoine, P. Carrette, R. Murenzi, and B. Piette, "Image analysis with two-dimensional continuous wavelet transform," *Signal Processing*, vol. 31, no. 3, pp. 241 – 272, 1993.

[83] A. Arnéodo, N. Decoster, and S. G. Roux, "A wavelet-based method for multifractal image analysis. i. methodology and test applications on isotropic and anisotropic random rough surfaces," *European Physical Journal B*, vol. 15, no. 3, pp. 567–600, 2000.

[84] F. van der Heijden, R. Duin, D. de Ridder, and D. M. J. Tax, *Classification, Parameter Estimation and State Estimation: An Engineering Approach Using MATLAB*. Wiley, 1st ed., Nov. 2004.

[85] B. van Ginneken and M. Loog, "Pixel position regression - application to medical image segmentation," in *Pattern Recognition, 2004. ICPR 2004. Proceedings of the 17th International Conference on*, vol. 3, pp. 718 – 721 Vol.3, aug. 2004.

[86] W. K. Pratt, *Digital Image Processing: PIKS Inside*. New York, NY, USA: John Wiley & Sons, Inc., 3rd ed., 2001.

[87] J. E. Bresenham, "Algorithm for computer control of a digital plotter," *IBM Systems Journal*, vol. 4, 1965.

[88] P. Pudil, J. Novovicova, and J. Kittler, "Floating search methods in feature-selection," *Pattern Recognition Letters*, vol. 15, no. 11, pp. 1119–1125, 1994.

[89] R. Gonzalez, R. Woods, and S. Eddins, *Digital Image Processing Using MATLAB*. Prentice Hall, 2nd ed., 2009.

[90] R. Newsom, C. Sinthanayothin, and J. Boyce, "Contrast Enhancement for Oral Fluorescein Angiograms," *British Journal of Ophthalmic Photographers (BJOP)*, 1998.

[91] C. Sinthanayothin, *Image analysis for automatic diagnosis of diabetic retinopathy*. PhD thesis, King's College of London, 1999.

[92] J. S. Lim, *Two-dimensional signal and image processing*. Upper Saddle River, NJ, USA: Prentice-Hall, Inc., 1990.

[93] Y. Lim and S. Lee, "On the color image segmentation algorithm based on the thresholding and the fuzzy c-means techniques," *Pattern Recognition*, 1990.

[94] A. P. Witkin, "Scale-space filtering," *Readings in computer vision: issues, problems, principles, and paradigms*, 1987.

[95] J.-F. Yang, S.-S. Hao, and P.-C. Chunge, "Color image segmentation using fuzzy C-means and eigenspace projections," *Signal Processing*, 2002.

[96] R. Krishnapuram and J. Keller, "A possibilistic approach to clustering," *IEEE Transactions on Fuzzy Systems*, 1993.

[97] B. Verma and P. Zhang, "A novel neural-genetic algorithm to find the most significant combination of features in digital mammograms," *Applied Soft Computing*, 2007.

[98] G. V. Dijck, M. M. V. Hulle, and M. Wevers, "Genetic algorithm for feature subset selectionwith exploitation of feature correlations from continuouswavelet transform: A real case application," *International Journal of Computational Intelligence*, 2004.

[99] J. Canny, "A computational approach to edge detection," *IEEE Transactions on Pattern Analysis and Machine Intelligence*, 1986.

[100] E. Erdem, A. Erdem, and S. Tari, "Edge strength functions as shape priors in image segmentation," *Energy Minimization Methods in Computer Vision and Pattern Recognition*, 2005.

[101] A. Hoover, V. Kouznetsova, and M. Goldbaum, "Locating blood vessels in retinal images by piecewise threshold probing of a matched filter response," *IEEE Transactions on Medical Imaging*, vol. 19, pp. 203–210, 2000.

[102] K. Zuiderveld, "Graphics gems iv," ch. Contrast limited adaptive histogram equalization, pp. 474–485, San Diego, CA, USA: Academic Press Professional, Inc., 1994.

[103] P. Massin, A. Erginay, and A. Gaudric, *Rétinopathie diabétique*. Atlas en imagerie médicale, Ed. scientifiques et médicales Elsevier, 2000.

[104] P. Soille, *Morphological Image Analysis: Principles and Applications*. Secaucus, NJ, USA: Springer-Verlag New York, Inc., 2nd ed., 2003.

[105] K. W. Tobin, E. Chaum, V. P. Govindasamy, and T. P. Karnowski, "Detection of anatomic structures in human retinal imagery," *IEEE Trans. Med. Imaging*, vol. 26, no. 12, pp. 1729–1739, 2007.

[106] A. D. Fleming, K. A. Goatman, S. Philip, J. A. Olson, and P. F. Sharp, "Automatic detection of retinal anatomy to assist diabetic retinopathy screening.," *Physics in Medicine and Biology*, vol. 52, no. 2, pp. 331–345, 2007.